

1-1-2009

Numerical Investigation Of Thermodiffusion Effects On PEM Fuel Cell Performance

Rihab. Jaralla
Ryerson University

Follow this and additional works at: <http://digitalcommons.ryerson.ca/dissertations>



Part of the [Mechanical Engineering Commons](#)

Recommended Citation

Jaralla, Rihab, "Numerical Investigation Of Thermodiffusion Effects On PEM Fuel Cell Performance" (2009). *Theses and dissertations*. Paper 1130.

**NUMERICAL INVESTIGATION OF
THERMODIFFUSION EFFECTS ON PEM FUEL CELL
Performance**

by
Rihab Jaralla, B.Eng.

University of Technology, IRAQ, 1993

A Thesis

presented to Ryerson University

in partially fulfillment of the requirements for the degree of

Master of Applied Science

in the Program of
Mechanical Engineering

Toronto, Ontario, Canada

© Rihab Jaralla, 2009

AUTHOR'S DECLARATION

I hereby declare that I am the sole author of this thesis.

I authorize Ryerson University to lend this thesis to other institutions or individuals for the purpose of scholarly research.

I further authorize Ryerson University to reproduce this thesis by photocopying or by other means, in total or in part, at the request of other institutions or individuals for the purpose of scholarly research.

ABSTRACT

Numerical Investigation of Thermodiffusion Effects on PEM

Fuel Cell Performance

Rihab Jaralla

Master of Applied Science, Ryerson University,

Department of Mechanical and Industrial Engineering, 2009

A novel mathematical model for an entire proton exchange membrane fuel cell (PEMFC) is developed with its focus placed on the modeling and assessment of thermodiffusion effects that have been neglected in previous studies. Instead of treating catalyst layers as interfaces of nil thickness, the model presented here features a finite thickness employed for catalyst layers, allowing for a more realistic description of electrochemical reaction kinetics arising in the operational PEMFC. To account for the membrane swelling effect, the membrane water balance is modeled by coupling the diffusion of water, the pressure variation, and the electro-osmotic drag. The complete model consisting of the equations of continuity, momentum, energy, species concentrations, and electric potentials in different regions of a PEMFC are numerically solved using the finite element method implemented into a commercial CFD (Comsol 3.4) code. Various flow and transport phenomena in an operational PEMFC are simulated using the newly developed model. The resulting numerical simulations demonstrate that the thermodiffusion has a noticeable impact on the mass transfer for the oxygen. It is also revealed through a systematic parametric study that, as the porosity of gas diffusion layers and catalyst layers increase, the current density of an operational PEMFC may increase. Also, it is found that a PEM fuel cell can perform better with reasonably high operating pressure and temperature, as well as a supply of fully humidified gaseous reactants.

ACKNOWLEDGEMENTS

I am sincerely grateful to Professor Jun Cao and Professor M. Z. Saghir of Ryerson University for their invaluable guidance, great support and encouragement during my graduate study. Without their guidance and suggestions the completion of this thesis would not have been possible.

I also would like to acknowledge the useful suggestions of my colleague Jianghui Yin.

I would like to dedicate this thesis to my family members, my husband Tawfiq Jaber; his constant encouragement and support is the best driving power of my work. I would also like to thank my beloved children: Mohamad, Ali and Hussain, as well as my parents, especially my mom for her generous love that is the most invaluable treasure of my life.

TABLE OF CONTENTS

AUTHOR'S DECLARATION	ii
ABSTRACT.....	iii
ACKNOWLEDGEMENTS.....	iv
TABLE OF CONTENTS.....	v
LIST OF TABLES	viii
LIST OF FIGURES	ix
NOMENCLATURE.....	xi
Chapter 1	1
Introduction and Literature Review	1
1.1 Fuel Cell Description	1
1.2 Polymer Electrolyte Membrane Fuel Cells (PEMFCs)	4
1.2.1 Membrane	7
1.2.2 Catalyst layer (CL).....	8
1.2.3 Gas Diffusion Layer (GDL).....	9
1.2.4 Bipolar Plates	9
1.3 Literature Review.....	11
1.4 thermodiffusion.....	22
1.5 Research Objectives.....	26
1.6 Thesis Organization	27
Chapter 2	28
Computer Model Description	28
2.1. Model assumptions	29
2.2. Modeling Equations in Gas Diffusion Layers (GDLs).....	30
2.2.1. Continuity and Momentum Equations	31

2.2.2. Mass Transport Equations.....	32
2.2.3. Solid-Phase Potential Equations	36
2.2.4. Energy equation	36
2.3. Modeling Equations in Catalyst Layers	37
2.3.1 Flow Model: Darcy's law	37
2.3.2. Electrochemical Modeling Equations	38
2.3. 3. Mass Transport Equations.....	39
2.3.4. Energy Equations	40
2.3.5. Solid-phase and membrane-phase potential equations	41
2.4. Modeling Equations in Membrane.....	42
2.4.1. Darcy's Law and Energy Equations	43
2.4.2. Water and Proton Transport Model	44
2.5. Collector plates	51
2.6. Boundary Conditions	52
2.6.1 Darcy's Law	53
2.6.2 Species Equations	54
2.6.3 Solid-Phase Potential Equation.....	54
2.6.4 Energy Equations	55
2.6.4 Boundary Conditions for Water and Proton Transport Model	55
2.7 Modeling Parameters	56
2.8 Numerical Solution Technique	59
Chapter 3.....	62
Base Case Results and Parametric Study.....	62
3.1 Model Validation	62
3.2 Base Case Study on thermodiffusion Effect.	65

3.2.1 Oxygen Distribution.....	65
3.2.2 Water Vapour Distribution at Cathode Side	67
3.2.3 Hydrogen and Water Vapour Distribution at the Anode Side	69
3.3. Parametric Study	70
3.3.1. Effect of Operating Pressure Load.....	70
3.3.2. Effect of temperature	73
3.2.3 Effect of Relative Humidity.....	75
3.3.4 Effect of GDL Porosity.....	78
3.3.5 Effect of Proton Conductivity.....	81
3.3.6 The effects of effective porosity of the catalyst layer.....	84
3.4 Effect of thermodiffusion on polarization curve.....	86
Chapter 4.....	91
Conclusions and Outlook.....	91
4.1 Conclusion	91
4.2 Contributions.....	92
4.3 Recommendations.....	93
REFERENCES	94

LIST OF TABLES

Table 2.1 Physical dimension of the PEM fuel cell,	57
Table 2.2 Operating parameters for a PEM fuel cell under a base case	57
Table 2.3 Electrode properties.....	58
Table 2.4 Electrochemical properties of a PEM fuel cell.....	59
Table 2.5 Binary diffusivities at 1atm and reference temperatures.	59

LIST OF FIGURES

FIGURE 1.1: THE POLYMER ELECTROLYTE FUEL CELL (PEMFC).	1
FIGURE 1.2: MAIN CELL COMPONENTS AND PROCESSES	6
FIGURE 1.3: ILLUSTRATION OF THE SORET EFFECT. IF A	24
FIGURE 2.1: SKETCH OF A SINGLE PEM FUEL CELL CONFIGURATION, [1].	28
FIGURE 2.2: TRANSPORT PATHS OF PROTONS AND ELECTRONS WITHIN	41
FIGURE 2.3: SCHEMATIC OF WATER TRANSPORT PHENOMENA IN A	45
FIGURE 2.4: SCHEMATIC DIAGRAM OF COMPUTATION MODEL OF A PEM FUEL.....	52
FIGURE 2.5: MESH OF THE COMPUTATIONAL DOMAIN.....	60
FIGURE 2.6: MESH QUALITY OF COMPUTATIONAL DOMAIN.....	61
FIGURE 3.1: COMPARISON OF MODELING RESULTS WITH	62
FIGURE 3.2: POWER CURVE RESULTING FROM THE FUEL CELL POLARIZATION CURVE..	64
FIGURE 3.3: OXYGEN MOLE FRACTION IN Y-Z PLANE FOR CELL	66
FIGURE 3.4: COMPARISON OF OXYGEN MOLE FRACTION WITH AND.	67
FIGURE 3.5: WATER VAPOUR MOLE FRACTION FOR CELL VOLTAGE	68
FIGURE 3.6: COMPARISON OF WATER VAPOR MOLE FRACTION WITH	68
FIGURE 3.7: WATER VAPOR MOLE FRACTION AT ANODE SIDE FOR CELL	69
FIGURE 3.8: COMPARISON OF WATER VAPOR MOLE FRACTION AT ANODE	70
FIGURE 3.9: CELL PERFORMANCES AT DIFFERENT OPERATING PRESSURE LOADINGS. ..	71
FIGURE 3.10: OXYGEN MOLE FRACTION DISTRIBUTION UNDER.	72
FIGURE 3.11: OXYGEN MOLE FRACTION PROFILE ACROSS THE	73
FIGURE 3.12: EFFECT OF TEMPERATURE ON FUEL CELL PERFORMANCE.	74
FIGURE 3.13: POLARIZATION CURVES CORRESPONDING TO	75
FIGURE 3.14: WATER CONTENT AT CELL VOLTAGE 0.6V, AND	76
FIGURE 3.15: MEMBRANE-PHASE POTENTIAL LOSSES AT CELL	77

FIGURE 3.16: OXYGEN MOLE FRACTION DISTRIBUTION INSIDE FUEL.....	79
FIGURE 3.17: OXYGEN MOLE FRACTION DISTRIBUTION INSIDE.	80
FIGURE 3.18: EFFECTS OF GDL POROSITY ON THE PEM FUEL CELL PERFORMANCE.	81
FIGURE 3.19: EFFECT OF PROTON CONDUCTIVITY ON PEM FUEL CELL	82
FIGURE 3.20: MEMBRANE-PHASE POTENTIAL LOSSES FOR DIFFERENT	83
FIGURE 3.21: THE INFLUENCE OF EFFECTIVE POROSITY ON THE PERFOR.....	84
FIGURE 3.22: OXYGEN MOLE FRACTION DISTRIBUTION IN THE CATHOD.	85
FIGURE 3.23: OXYGEN MOLE FRACTION PROFILE ACROSS THE CHANNE.....	86
FIGURE 3.24: COMPARISON OF MODELING RESULTS WITH AND WITHOU	87
FIGURE 3.25: COMPARISON OF MODELING RESULTS WITH AND WITHOUT.	87
FIGURE 3.26: COMPARISON OF MODELING RESULTS WITH AND WITHOUT	88
FIGURE 3.27: COMPARISON OF MODELING RESULTS WITH AND WITHOUT	89
FIGURE 3.28: COMPARISON OF MODELING RESULTS WITH AND WITHOUT	89
FIGURE 3.29: COMPARISON OF MODELING RESULTS WITH AND WITHOUT	90

NOMENCLATURE

- a catalyst surface area per unit volume (m^2/m^3)
- A_{MEA} full active MEA area (m^2)
- c concentration (mole fraction, or mass fraction) (-)
- C electric charge (Coulomb)
- C Concentration (mol/m^3)
- C_p specific heat capacity at constant pressure ($J/kg/K$)
- D diffusion coefficient (m^2/s)
- D^T thermal diffusion coefficient ($m^2/s/K$)
- e membrane constant (mol/m^3)
- E potentiel (Volt)
- EW_m equivalent molecular weight of the membrane (kg/mol)
- f swelling coefficient of membrane (-)
- F Faraday's constant 96487 (C/mol)
- i current density (A/m^2)
- I current (A)
- j_0^{ref} exchange current density (A/m^2)
- k thermal conductivity ($W/m/K$)
- k_ϕ electro-kinetic permeability (m^2)
- k_h hydraulic permeability (m^2)
- k_p permeability of electrode/membrane (m^2)

M	molecular weight of mixture (kg/mol)
M_i	molecular weight of component i (kg/mol)
n	molar number of electrons transferred (-)
n_d	electro-osmotic drag coefficient (-)
N	molar flux ($mol/m^2/s$)
P	pressure (Pa)
R	universal gas constant 8.3145 ($J/mol/K$)
RH	Relative Humidity (-)
S	mass source/sink ($kg/m^3/s$)
T	temperature (K)
V	cell potential ($Volt$)
\vec{v}	velocity vector (m/s)
w	power ($Watt$)
x	molar fraction (mol/m^3)
y	y axis (m)
z	z axis (m)
Z	charge number (-)

GREEK SYMBOLS

α	transfer coefficient (-)
ε	porosity (-)
ε_w^m	volume fraction of water (-)
η	overpotential ($Volt$)

λ	membrane water content (-)
μ	viscosity ($kg/m/s$)
ρ	density (kg/m^3)
ω	mass fraction (-)
ϕ	electric potential (<i>Volt</i>)
θ	volume fraction of membrane in the catalyst layer (-)
χ	cell efficiency (-)
σ	electrical conductivity (S/m)

SUBSCRIPTS

a	Anode
act	Activation
c	Cathode
e	Equilibrium state
f	Fixed charge
g	Gas phase
i	Species i
ij	Gas pair i, j in a mixture
mem	Membrane
l	Liquid phase
ohm	Ohmic
m	Membrane phase
rev	Reversible
s	Solid phase
w	Water

0 Reference conditions

SUPERSCRIPTS

eff Effective value of parameter

ref Reference value

sat Saturation state

T Thermal

0 Standard state

Chapter 1

Introduction and Literature Review

1.1 Fuel Cell Description

Fuel cells are a family of electrochemical devices that convert chemical energy of the reactants directly into DC electricity and heat with high efficiency. In general, a fuel cell is simply an energy conversion device for power generation where reactants are supplied. The basic physical structure of a fuel cell consists of an electrolyte membrane layer in contact with a porous anode and cathode on either side. A schematic representation of a fuel cell with reactant/product gases and the ion conduction flow directions through the cell is shown in Figure 1.1.

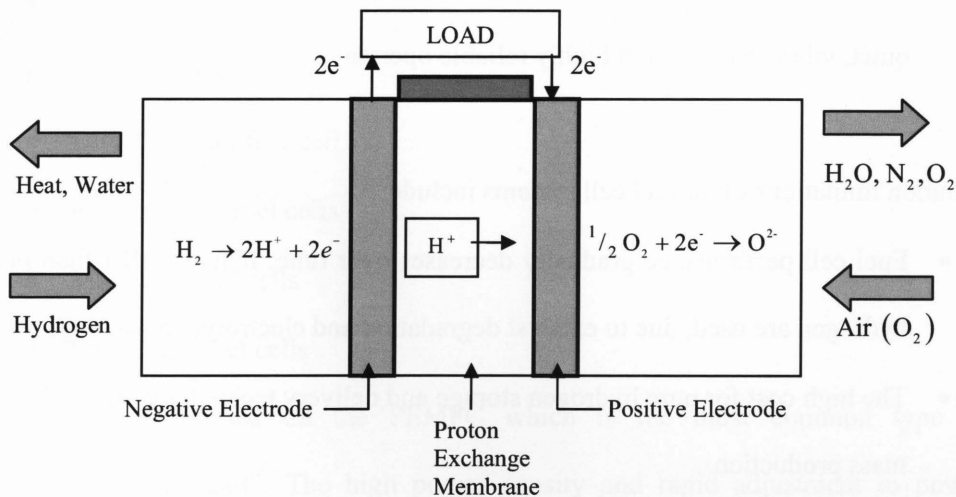


Figure 1.1: The polymer electrolyte fuel cell (PEMFC) [4].

In a characteristic fuel cell, gaseous fuels are supplied continuously to the anode (negative electrode); while an oxidant (oxygen from the air) is supplied continuously to the cathode (positive electrode). An electric current is generated via

electrochemical reactions with the aid of two catalyst layers inserted between the central membrane and the electrodes at the two sides. The main advantages of fuel cell systems include:

- Fuel cells generate by-products: waste heat and water; thus, they produce zero or near-zero greenhouse emissions.
- Fuel cells have the potential for a high operating efficiency
- Many types of potential fuel sources are available.
- Fuel cells have a highly scalable design.
- Compared with batteries, fuel cells provide nearly instantaneous recharge capability.
- Fuel cells generate electricity in a single step without any moving parts (other than pumps or compressors in some fuel cell plant subsystems), allowing for quiet, vibration-free, and highly reliable operation.

Common limitations of all fuel cell systems include:

- Fuel cell performance gradually decreases over time, if fuels other than pure hydrogen are used, due to catalyst degradation and electrolyte poisoning.
- The high cost for pure hydrogen storage and delivery technology affects the mass production.
- Fuel reformation technology needs to be considered, if pure fuel is not used.

Many types of fuel cells are currently being investigated. These types are differentiated from one another on the basis of the electrolyte and/or fuel employed.

The most common fuel cell types are:

- Polymer electrolyte membrane fuel cells (PEMFCs)

- Alkaline fuel cells (AFCs)
- Phosphoric acid fuel cells (PAFCs)
- Solid oxide fuel cells (SOFCs)
- Molten carbonate fuel cells (MCFCs)
- Direct methanol fuel cells (DMFCs)
- Zinc air fuel cells (ZAFCS)
- Protonic ceramic fuel cells (PCFCs)
- Biological fuel cells (BFCs)

When conducting research on fuel cell types, one may also come across the names of other fuel cells, such as:

- Direct borohydride fuel cells
- Metal hydride fuel cells
- Formic acid fuel cells
- Direct ethanol fuel cell
- Regenerative fuel cells
- Microbial fuel cells
- Enzymatic fuel cells

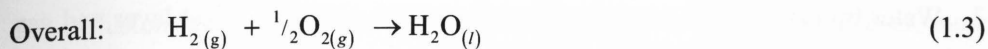
This research focused on the PEMFC which is the most common type of “regenerative fuel cell”. The high power density and rapid adjustment to power demands make proton exchange membrane fuel cells (PEMFCs) one of the best candidates for a clean alternative energy source in the 21st century, especially for transportation applications.

1.2 Polymer Electrolyte Membrane Fuel Cells (PEMFCs)

The polymer electrolyte membrane fuel cells (PEMFCs), sometimes also referred to as proton exchange membrane fuel cells, deliver high power density while providing low levels of cost, weight and volume. A PEMFC consists of a negatively charged electrode (anode), a positively charged electrode (cathode), and an electrolyte membrane, as shown in Figure 1.1. Hydrogen is oxidized at the anode and oxygen is reduced at the cathode. Protons are transported from the anode to the cathode through the electrolyte membrane, and the electrons are carried over an external circuit load. At the cathode oxygen reacts with protons and electrons, generating water and producing heat.

In the PEM fuel cell, transport from the fuel flow channels to the electrode takes place through an electrically conductive carbon paper, which covers the electrolyte on both sides. These backing layers typically have a porosity of 0.3 to 0.8 and serve to transport the reactants and products to and from the bipolar plates to the reaction site [1]. An electrochemical oxidation reaction at the anode produces electrons that flow through the bipolar plate/cell interconnect to the external circuit, while the ions pass through the electrolyte to the positive electrode (cathode). The electrons return from the external circuit, while the ions pass through the electrolyte to the positive electrode. The electrons return from the external circuit to participate in the electrochemical reduction reaction at the cathode as shown in Figure 1.1. The reactions at the electrodes are:





where “(g)” refers to the gaseous state, “(aq)” stands for a substance in the aqueous phase that is dissolved in water [2], and “(l)” denotes the liquid state.

The standard electrolyte material presently used in PEM fuel cells is a fully fluorinated Teflon-based material produced by DuPont for space applications in the 1960s. The DuPont electrolytes have the generic brand name Nafion, and the types used most frequently are 1135, 115, and 117, the latter of which is the one used in this study. The Nafion membranes are fully fluorinated polymers that have very high chemical and thermal stability. The electrodes are thin films that are bonded to the membrane. Electrodes with low platinum loading perform as well or better than high-platinum-loaded electrodes. To improve the utilization of platinum, a soluble form of the polymer is incorporated into the porosity of the carbon support structure. This increases the interface between the electrocatalyst and the solid polymer electrolyte.

The following processes take place inside the fuel cell (the numbers correspond to those in Figure 1.2) [3]:

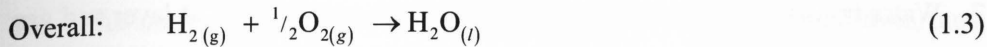
1. Gas flow through the channels; some convective flows may be induced in the porous layers.
2. Gas diffusion through porous media.
3. Electrochemical reactions, including all the intermediary steps.
4. Proton transport through proton-conductive polymer membrane.
5. Electron conduction through electrically conductive cell components.
6. Water transport through polymer membrane including both electrochemical drag and back diffusion.

1.2 Polymer Electrolyte Membrane Fuel Cells (PEMFCs)

The polymer electrolyte membrane fuel cells (PEMFCs), sometimes also referred to as proton exchange membrane fuel cells, deliver high power density while providing low levels of cost, weight and volume. A PEMFC consists of a negatively charged electrode (anode), a positively charged electrode (cathode), and an electrolyte membrane, as shown in Figure 1.1. Hydrogen is oxidized at the anode and oxygen is reduced at the cathode. Protons are transported from the anode to the cathode through the electrolyte membrane, and the electrons are carried over an external circuit load. At the cathode oxygen reacts with protons and electrons, generating water and producing heat.

In the PEM fuel cell, transport from the fuel flow channels to the electrode takes place through an electrically conductive carbon paper, which covers the electrolyte on both sides. These backing layers typically have a porosity of 0.3 to 0.8 and serve to transport the reactants and products to and from the bipolar plates to the reaction site [1]. An electrochemical oxidation reaction at the anode produces electrons that flow through the bipolar plate/cell interconnect to the external circuit, while the ions pass through the electrolyte to the positive electrode (cathode). The electrons return from the external circuit, while the ions pass through the electrolyte to the positive electrode. The electrons return from the external circuit to participate in the electrochemical reduction reaction at the cathode as shown in Figure 1.1. The reactions at the electrodes are:





where “(g)” refers to the gaseous state, “(aq)” stands for a substance in the aqueous phase that is dissolved in water [2], and “(l)” denotes the liquid state.

The standard electrolyte material presently used in PEM fuel cells is a fully fluorinated Teflon-based material produced by DuPont for space applications in the 1960s. The DuPont electrolytes have the generic brand name Nafion, and the types used most frequently are 1135, 115, and 117, the latter of which is the one used in this study. The Nafion membranes are fully fluorinated polymers that have very high chemical and thermal stability. The electrodes are thin films that are bonded to the membrane. Electrodes with low platinum loading perform as well or better than high-platinum-loaded electrodes. To improve the utilization of platinum, a soluble form of the polymer is incorporated into the porosity of the carbon support structure. This increases the interface between the electrocatalyst and the solid polymer electrolyte.

The following processes take place inside the fuel cell (the numbers correspond to those in Figure 1.2) [3]:

1. Gas flow through the channels; some convective flows may be induced in the porous layers.
2. Gas diffusion through porous media.
3. Electrochemical reactions, including all the intermediary steps.
4. Proton transport through proton-conductive polymer membrane.
5. Electron conduction through electrically conductive cell components.
6. Water transport through polymer membrane including both electrochemical drag and back diffusion.

7. Water transport (both vapor and liquid) through porous catalyst layer and gas diffusion layers.
8. Two-phase flow of unused gas carrying water droplets.
9. Heat transfer, including both conduction through solid components of the cell and convection to reactant gases and cooling medium.

It is important to understand those processes, their mutual interdependence, and their dependence on components design and materials properties. Design of the components and properties of materials must accommodate the aforementioned processes with minimum obstruction and losses. Moreover, more than one process occurs in some of the components frequently with conflicting requirements, the PEMFC structure design and material selections must be optimized. For instance, the gas diffusion layer (GDL) must be optimized so that the reactant gas may easily diffuse and, meanwhile, the water traveling in the opposite direction does not accumulate in the pores.

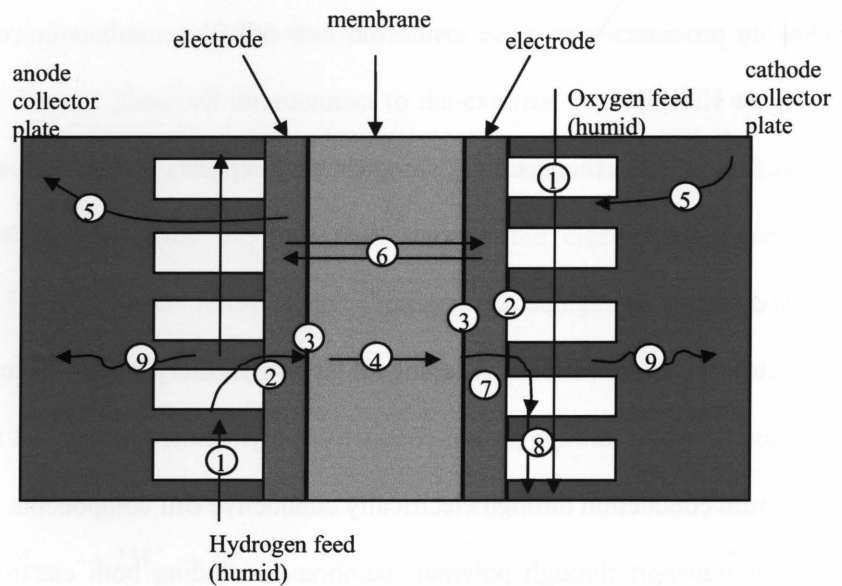


Figure 1.2: Main cell components and processes.

The diffusion layer, sometimes also referred to as the current collector layer, must be both electrically and thermally conductive [2]. The same requirements may be established for almost every fuel cell component. A fuel cell seems to be a very simple device; however, many processes occur simultaneously.

1.2.1 Membrane

A fuel cell membrane must exhibit relatively high proton conductivity, present an adequate barrier to mixing of fuel and reactant gases, and operate chemically and mechanically stably in the fuel cell environment. Typically, the membranes for PEM fuel cells are made of perfluorocarbon-sulfonic acid ionmer (PSA). This is essentially a copolymer of tetrafluoroethylene (TFE) and various perfluorosulfonate monomers. The best-known membrane material is NafionTM made by Dupont, which uses perfluoro-sulfonylfluoride ethyl-propyl-vinyl ether (PSEPVE) [4].

The protonic conductivity of the membrane is strongly dependent on membrane structure and its water content. The water content in the membrane is usually expressed as grams of water per gram of polymer dry weight, or as number of the water molecules per sulfonic acid groups present in the polymer, $\lambda = N(\text{H}_2\text{O})/N(\text{SO}_3\text{H})$. The maximum amount of water in the membrane strongly depends on the state of water used to equilibrate the membrane. Water uptake from the vapour phase may be more relevant for fuel cell operation, where the reactant gases are humidified and water is present in the vapour phase. Water uptake results in the membrane swelling and changes its dimensions, which is a very significant factor for fuel cell design and assembly.

1.2.2 Catalyst layer (CL)

A fuel cell electrode is essentially a thin catalyst layer pressed between the ionomer membrane and porous, electrically conductive substrate. It is the layer where the electrochemical reactions take place. More precisely, the electrochemical reactions take place on the catalyst surface. Transport phenomena in the catalyst layer are complicated due to the electrochemical reactions.

The catalyst layer usually consists of platinum, carbon, membrane material, and Teflon. The most common catalyst in PEM FC for both oxygen reduction and hydrogen oxidation reactions is platinum. In the early days of PEMFC development, large amounts of Pt catalyst were used (up to 28 mg cm^{-2}). In the late 1990s, with the use of supported catalyst structure, this was reduced to $0.3\text{-}0.4 \text{ mg cm}^{-2}$. It is the catalyst surface area that matters, not the weight, so it is important to have small platinum particles (4nm or smaller) with a large surface area finely dispersed on the surface of catalyst support, typically carbon powders (cca 40 nm) with a high mesoporous area ($>75 \text{ m}^2\text{g}^{-1}$). Typical support material is Vulcan XC72R BY Cabot, but other carbons such as Black Pearls BP 2000, Ketjen Black Intl., or Chevron Shawinigan have been used [4].

Catalyst layers are made highly porous, thus their active surface areas are orders of magnitudes greater than their geometrical ones. The requirements of a catalyst layer are: high intrinsic activity, large active surface area, high ionic and electric conductivities, highly porous for reactant access and product removal, and stability.

1.2.3 Gas Diffusion Layer (GDL)

In a fuel cell, a gas diffusion layer is compressed to minimize the contact resistance loss. Both carbon papers and carbon cloths are relatively soft and easily deformable materials. Cloth is more compressible than paper.

The catalyst layer consists of carbon or graphite particles mixed with PTFE binder. The resulting pores are between 0.1 and 0.5 μm , thus much smaller than the pore size of the carbon fiber papers (20-50 μm). The small pore size helps in improving the electrical contacts with the adjacent catalyst layer. The interface with the adjacent catalyst layer may also be fitted with a coating or a micro porous layer to ensure better electrical contacts as well as efficient water transport in and out of the diffusion layer.

One of the functions of the gas diffusion layer is to connect electrically the catalyst layer with the bipolar plate. Because only a portion of the bipolar plate makes the contact (the other portion is open for access of reactant gases), the gas diffusion layer bridges the channels and redistributes electrical current. Because of this, both through-plane and in plane resistivities of gas diffusion material is important [4].

1.2.4 Bipolar Plates

For a single PEM fuel cell, there are no bipolar plates (only single-sided flow-field plate). The two plates on each side of the membrane electrode assembly may be considered as two halves of a bipolar plate. In fuel cells with more than one cell, there is at least one bipolar plate. Bipolar plates perform many roles in fuel cells. The fully

functioning bipolar plates are essential for multicell configurations, by electrically connecting the anode of one cell to the cathode of the adjacent cell.

The bipolar collector /separator plates have several functions in a fuel cell stack. Their required properties follow their functions, namely:

- They separate the gases in adjacent cells; therefore, they must be impermeable to gases.
- They typically house the flow field channels; therefore, they must be conformable.
- They provide structural support for the stack; therefore, they must have adequate strength, yet they must be lightweight.
- They connect cells electrically in series; therefore, they must be electrically conductive.
- They conduct heat from active cells to the cooling cells or conduits; therefore, they must be thermally conductive.

In addition, they must be corrosion resistant in the fuel cell environment, yet they must not be made out of “exotic” and expensive materials. One of the first materials used for PEM fuel cell bipolar plates was graphite primarily because of its demonstrated chemical stability in the fuel cell environment. Graphite is inherently porous, which may be detrimental in fuel cell applications. Those plates therefore must be impregnated to make them impermeable. This material is still used in laboratory fuel cells (primarily in single cells). However, machining of graphite plates is not an easy task and may be prohibitively expensive for most fuel cell applications.

It should be mentioned that one fuel cell manufacturer (UTC Fuel Cells) uses porous graphite plates for water management inside the fuel cell stack.

In general, two families of materials have been used for fuel cell bipolar plates, namely, graphite based (including graphite/composite) and metallic [4].

1.3 Literature Review

Modeling plays a significant and important role in the fuel cell design and the development process. Because of its importance, modeling is initiated early into a fuel cell development cycle. Hence, modeling has a critical role in the fuel cell design and development process. A designer can use an accurate and robust model to design and develop fuel cell stacks more efficiently and often with better performance and lower manufacturing cost. Using fuel cell modeling as a successful design tool requires the model to be robust, accurate, and able to provide usable answers quickly. In terms of robustness, the model should be able to predict fuel cell performance under a large range of operating conditions. For example, a PEM fuel cell can be operating at different temperatures, humidity levels, and fuel mixtures. A robust model should be able to predict fuel cell performance under varying conditions. The model must also predict fuel cell performance accurately.

There are an enormous number of fuel cell analytical /numerical studies. The simple way to classify these models is to classify them into two major groups: the microscopic models that simulate the transport phenomenon on a pore or microscopic level, and the macroscopic models that study of the fuel cell operation using average parameters. Microscopic models are realistic, but such models require more detailed

information of the microstructures which are not readily available, and the computation time is much longer for the microscopic models. Therefore, nowadays most of the existing models for PEM fuel cell are of macroscopic nature.

The macroscopic models for fuel cells can be further classified according to the objects of study: a single-fuel-cell unit, a stack, and a system. A stack contains a number of fuel cells arranged in a matrix so as to produce the desired power output. A system is a power production unit which includes the fuel cell stack and peripherals such as supply systems, heat exchangers, power controls, etc. A single fuel cell unit usually contains a cathode, a membrane assembly, and an anode. This review focuses mainly on macroscopic models for a single PEM fuel cell.

Since the early nineties, many papers on single PEM fuel cell models have been published to investigate different aspects of the heat and mass transport processes in the fuel cell. Springer *et al.* [5] and Bernardi *et al.* [6] were the first to publish complete fuel cell models which are isothermal, one-dimensional, and steady state, but one-dimensional models are unable to simulate the species and phase distribution along the channel within the gas diffusion layer (GDL). In late nineties, the models were more advanced, involving multi-dimensionality (2D or 3D), multiphase flow, and entire fuel cell structure. Illustrated below is a brief overview of the modeling strategies employed by some of the models reported in the literature. Some of these modeling approaches were used in this work.

A two dimensional model for an entire sandwich of PEM fuel cell including the gas channels was developed by Gurau *et al.* [7]. The self-consistent model for porous

media was used for the equations describing transport phenomena in the membrane, catalyst layers, and gas diffusers, while standard equations of Navier-Stokes, energy transport, continuity, and species concentrations were solved in the gas channels.

With a special treatment of the transport equations they managed to use the same numerical method in the unified domain consisting of the gas channels, gas diffusers, catalyst layers and membrane. It also eliminated the need to prescribe arbitrary or approximate boundary conditions at the interfaces between different parts of the fuel cell sandwich. The only input data were the parameters that can be controlled in real fuel cell applications. No assumptions were necessary for the distribution of the species concentrations or current density, which is distinguished from other fuel cell models available in the literature relying on assumptions for a number of parameters.

By solving transport equations as well as the equations for electrochemical reactions and current density with the membrane phase potential, polarization curves under various operating conditions were obtained. Oxygen and water vapor mole fraction distributions in the coupled cathode gas channel-gas diffuser were studied for various operating current densities. And they found that the computed oxygen mole fraction along the gas channel-gas-diffuser interface and the current density along the membrane-catalyst layer interface do not present linear distributions, as were assumed in other works. The oxygen mole fraction field is also presented in the coupled gas channel-gas-diffuser domain. Liquid water velocity distributions in the membrane and influences of various parameters on the cell performance were also obtained. The computed fuel cell performances were realistic.

Zhou *et al.* [8] and Um *et al.* [9] developed a three-dimensional model using a similar approach by Gurau *et al.* A general three-dimensional model for PEMFCs has been proposed in [8] and numerical simulations have been performed to evaluate the effects of various design operating parameters on fuel cell performances. In Gurau *et al.* , the unified approach was applied to three distinct unified domains. In that work, the unified approach was significantly extended to treat the whole fuel cell sandwich as one unified domain which includes two flow channels, two gas diffusers, two catalyst layers, and a membrane. This general mathematical model consists of the equations of continuity, momentum, energy, and species concentrations in different elements of the fuel cell sandwich, as well as the equations for phase potential in the membrane and the catalyst layer. This set of governing equations is coupled with chemical reaction kinetics by introducing various source terms. They found that once the model is further developed into dimensionless forms, the similarity of the governing equations in different components are obvious and, with special treatment, the general mathematical model can be solved in coupled domains without prescribing any boundary conditions at various interfaces between the different components of the fuel cell sandwich.

For generality, the effects of various dimensionless parameters on fuel cell performance can be evaluated. Another manifestation of the generality of the model lies in its independence of chemical kinetics models, since the kinetics are incorporated in the source terms. One can choose any kinetics models, and any new development in the electrochemistry can easily be incorporated in this general model. The predicted polarization curve agrees very well with the experimental result. By comparing with the 2-D case, this 3-D model has produced more accurate results,

especially at high current densities, as it has included the added mass resistance brought by the collector plate. The modeling results indicated that their 3-D model could be a valuable tool for fuel cell design, optimization and operation.

Transport phenomena of mass, energy, momentum and electrical charges play a significant role in proton exchange membrane fuel cells (PEMFCs). The transport and balance equations are the basis of a simulation model by Costamagn [10], which allows the evaluation of the distribution of the physico-chemical parameters within the structure of a PEMFC reactor. The validated model was then used to investigate the behaviour of the reactor, with particular attention paid to critical operating conditions.

Some critical aspects need to be accurately verified. In particular, for an operating polymeric membrane; both the temperature and the hydration level have to be carefully controlled in order to obtain satisfactory performance. Costamagn found that local temperature peaks above 130°C (at 1 atm) cause irreversible degradation of the membrane, while local dehydration leads to a reversible decrease of the efficiency of the conversion process. In addition, water condensation in the gas distributor can lead to the occlusion of some gas channels, causing periodical interruptions of the operation of the system. A model based on the study of charge, mass, momentum and energy transport within the PEMFC has been studied and validated on the basis of the experimental data. Costamagn's model allowed the identification of the distribution of the physico-chemical parameters within the reactor; in particular, the zones of the cell where membrane dehydration and water condensation occur have been shown and discussed in this study. Thus, this model can act as the basis for a study of the optimal

fuel cell geometry and operating parameters which could alleviate the critical aspects of the PEMFC modeling study.

An analysis of transport phenomena in a proton exchange membrane fuel cell (PEMFC) was presented by Djilali and Lu [11], with focus placed on the modeling and assessment of non- isothermal and non- isobaric effects. The model takes into account diffusion of humidified fuel and oxidant gases through the porous electrodes, water transport through the electrodes and membrane, as well as heat transfer and gas pressure gradients in the fuel cell. The micro-hydrodynamic phenomena associated with small electrode permeability were also taken into account. The model was implemented in a 1-D code, and solved numerically to analyze fuel cell performance and water transport over a range of operating current densities.

A parametric study was performed by Djilali and Lu and results compared and validated against available data. Non-uniform temperature and pressure distributions were found to have a large impact on the predicted liquid water and vapour fluxes in the anode and cathode diffusion layers. The model yielded more conservative humidification requirements than indicated by isothermal/isobaric models. Assuming fully hydrated conditions are maintained, polarization is not affected significantly by temperature and pressure non-uniformity. Finally, it was found that, in the range of permeabilities of the porous electrodes used in PEMFCs (10^{-16} - 10^{-17} m²), Knudsen diffusion has to be taken into account in modeling gas transport.

Siegel [12] carried out a two-dimensional, non-isothermal, two-phase flow model of a porous cathode gas diffusion layer of a polymer- electrolyte-membrane fuel cell

taking in account the thermodiffusion. He solved this model numerically using computational fluid dynamics coding and sequentially solver scripting. The model accounted for multicomponent species diffusion. Phase change and transport of water were accounted for in terms of liquid phase water saturation level. The heat transfer was investigated for the fluids and solid matrix temperature separately. This study showed that the presence of liquid phase water reduces the performance of a cell, especially at high current densities. It was shown that its dominating parameters are capillary pressure and permeability. The performance of cathode increases with higher temperature and using higher GDL porosities. The average liquid phase water saturation level is reduced but it was found that the average current density only increases slightly.

To understand the interactions of electrochemical and thermal processes along with two-phase flow, Siegel used two equations to describe the thermal behavior. The average temperature difference between the fluids and the solid matrix is much smaller when using higher heat transfer coefficients. The maximal temperature is found to be present at the catalyst layer interface. The local hot spot position depends on the value of the heat transfer coefficient. It is seen that a one-phase model always overpredicts the fluids temperature.

Built upon the work of Cao *et al.* [13], a more general detailed non-isothermal, two-dimensional CFD model was presented by Yin [14] using Famlab, a commercial CFD package. In this model, with a finite thickness of catalyst layer taken into account, electrochemical reactions, including hydrogen oxidation reaction in the anode catalyst layer and oxygen reduction reaction in the cathode catalyst layer, were taken into

account by adding proper sources/sink terms in the governing equations. The water balance in the membrane was modeled by coupling diffusion of water, pressure variation, and the electro-osmotic drag. The membrane swelling effect was explicitly considered the newly derived model, leading to a set of novel water and proton transport equations for a membrane under the partial hydration condition. The electron transport in the catalyst layers, gas diffusion layers and bipolar plates were also described. The simulation using this model provided valuable information about the transport phenomena inside the PEM fuel cell such as the flow field, reactant gases distribution, temperature distribution, water content distribution, as well as the membrane-phase and solid-phase potential distributions. A parametric study was also performed that reveals the effect of various operation and property parameters on the fuel cell performance. Also, the model can be slightly modified to simulate various transport process within a cross section of the fuel cell. Along this new investigation direction, the superiority of the interdigitated flow field design was demonstrated over the conventional one. Good overall agreement was achieved when comparing numerical results based on the model and the available experimentally obtained data.

On the other hand, in the extension of the 2-D model presented by Cao *et al.*, a three-dimensional PEM fuel cell model was developed by Wu [15]. Taking into account the diffusion of water, the pressure variation, and the electro-osmotic drag in the membrane and using an empirical relationship between electro-osmotic drag and water content, a transport equation for membrane water molar concentration was obtained, and a new equation for the electric potential that strictly accounts for variable water contents was derived. It was also found that the new potential equation is more accurate than the conventionally employed Laplace's equation. The model is

capable of predicting the bulk flow velocity background, the distribution of reactant gases, temperature, local current density, membrane water concentration and membrane potential loss. A number of 3-D numerical simulations are performed for comparing the new model with other results obtained computationally or experimentally. The relationship between the humidity in fuel cell and the electric potential loss within the membrane was also investigated at different nominal current densities. The impact and importance of three-dimensionality, relative humidity, temperature, and pressure non-uniformity were assessed and discussed. Parametric studies were performed using the 2D model, which revealed the effect of various operating conditions on the fuel cell performance.

A comprehensive non-isothermal, three-dimensional, steady-state computational model of a polymer electrolyte membrane (PEM) fuel cell has been developed by Berning *et al.* [16]. The model incorporated a complete cell with both the membrane-electrode-assembly (MEA) and the gas distribution flow channels. With the exception of phase change, the model accounts for all major transport phenomena. The model was implemented into a computational fluid dynamics code, and simulations were presented with an emphasis on the physical insight and fundamental understanding afforded by the detailed three-dimensional distributions of reactant concentrations, current densities, and temperature and water fluxes. One of the major advantages of using a detailed model is to illustrate the detailed distribution of the reactant gases inside the fuel cell. Such distributions, which cannot be measured in situ, provided valuable information about the onset of concentration losses and their effect on the limiting current density.

The results showed that significant temperature gradients exist within the cell, with temperature differences of several degrees K within the MEA. The three-dimensional nature of the distribution of flow velocities, species concentration, mass transfer rates, electric current and temperature was clearly illustrated by the simulations. And it was found that the transport is particularly pronounced under the collector plates land area and has a major impact on the current distribution and the limiting current density.

Sun *et al.* [17] have proposed a two-phase flow model for a PEM fuel cell using a similar treatment as in You *et al.* [18]. The model was based on the mixture flow model and the unified approach was used. Instead of using a separate model for the catalyst layer, the catalyst layers were included in the respective unified domains for the cathode and anode so that boundary conditions at the interface between the catalyst layer (CL) and gas diffuser layer (GDL) are no longer needed. The model coupled the flows, species, electrical potential, and current density distributions in the cathode and anode fluid channels, gas diffusers, catalyst layers and membrane respectively. Also, the two-phase flow model was used in the anode side, and the momentum transfer between the liquid and gas phases due to phase change was taken into consideration. Experiments have been conducted to study the performances of a PEM fuel cell and the results were used to improve and validate the model. The model was used to study the influences of fuel cell operating temperature, operating pressure and humidification temperature on the oxygen, vapour and liquid water transports, as well as fuel cell performances. Specifically the results of water distribution across different parts of a fuel cell were presented. And it was found that, in the cathode catalyst layer, total water mass fraction increases from its interface with the GDL to its interface with the catalyst layer. Within reasonably high temperature range and

with sufficient humidification for gas stream, total water mass fraction in the cathodic catalyst layer and the membrane ionic conductivity will both increase, leading to a better cell performance. The total water mass fraction in the cathode catalyst layer and the liquid volumetric fraction (liquid saturation) in the cathode channel and GDL increase with operating pressure due to higher water generation rate and lower vapour fraction in the gas phase. For counter-flow arrangement, generally, total mass fraction and liquid water volumetric fraction in the anode GDL and catalyst layer increases along the anode flow direction.

Baschuk and Li [19] presented a comprehensive, consistent and systematic mathematical model of PEM fuel cells that can be used as the general formulation for the simulation and analysis of PEM fuel cells. The general PEM fuel cell model formulation, which has been previously published by You *et al.*, was implemented for a two-dimensional fuel cell, assuming steady-state and isothermal operation. Water was assumed to exist only in the gas phase in the pores of polymer electrolyte layer. Water and ion transport was modeled using the generalized Stefan-Maxwell equations, with mobile species being water and hydronium. The governing equations were solved using the finite volume method with computer codes developed in house.

Baschuk and Li's simulation results illustrated three important phenomena in PEM fuel cells. The gas phase flow in the gas flow channels, electrode backing and catalyst layers showed that there is a net mass transport from the anode side of the cell to the cathode side. This net mass transport creates a bulk velocity that favors hydrogen transport from the gas flow channels to the anodic catalyst layer, but inhibits the flow of oxygen to the cathode reaction sites. Water is consumed in the anode catalyst layer

and produced in the cathodic catalyst layer. Some of the water required by the anode is transported from the cathode to the anode through the polymer electrolyte. However, the gas phase of the anode side supplies the majority of the water, making operation with fully humidified reactants necessary. The length of the gas flow channel has a significant effect on the current production of the PEM fuel cell, with a longer channel length having a lower performance relative to a shorter channel length. This lower performance is caused by a greater water content variation in the fuel cell with the longer channel length.

A number of thermal PEMFC models have appeared in the literature. The common goal was to better understand and hence optimizing fuel cell systems. Such information has been sought through modelling and simulation in order to get better understanding of water and species transport, optimize thermal management and shorten the design and optimization cycles. Recent models for PEM fuel cell were in the direction of two-phase, completely three-dimensional, realistic large-scale simulations with coupled electrochemical-transport-thermal effects.

1.4 Thermodiffusion

Diffusion is the net action of matter (particles or molecules), heat, momentum, or light towards minimizing their concentration gradient [20]. There are many kinds of diffusion mechanisms. Concentration diffusion or molecular diffusion is the tendency to mix due to concentration gradient in the system. Thermodiffusion is the tendency of a convection free mixture to separate under a temperature gradient. Pressure diffusion is the separation resulting from a pressure gradient. Forced diffusion is caused by unequal external forces acting on the chemical species. In this study, concentration diffusion and thermodiffusion are considered. For multicomponent gas

mixtures at moderate pressures, the Maxwell-Stefan equations in the form developed by Curtiss and Bird [21] will be used to model the transport of reactants in the electrodes.

If the temperature of a liquid mass varies with spatial position, there will be a transport of energy from the hotter regions to the colder ones, [22] as shown in Figure 1.3. A temperature gradient applied to a liquid mixture not only causes a heat flux but also gives rise to a diffusion current of constituent components. The resulting separation of the components causes a concentration gradient parallel or antiparallel with respect to the temperature gradient. This cross-effect between temperature and concentration is known as thermodiffusion or Ludwig-Soret-effect, since this effect was discovered by Ludwig [23] and systematically investigated by Soret [24] for liquid mixtures.

In response to the thermal gradient, concentration gradients appear in an originally uniform mixture. They produce isothermal diffusion, which aims at eliminating concentration variations. A steady state is reached when the separating effect of thermodiffusion is balanced by the remixing effect of isothermal diffusion [25]. For binary mixtures of dilute gases, it was found by experiment that the species with the larger molecular weight usually goes to the colder region, see Figure 1.3. If the molecular weights are about equal, then usually the species with larger diameter moves to the colder region. In some instances, there is a change in the sign of the thermodiffusion ratio as the temperature is lowered: when Soret coefficient is positive species A moves toward the colder region, and when it is negative, species A moves toward the warmer region [26]. For binary mixtures, the Soret effect is measured by

the Soret coefficient, which is defined as the ratio of the thermodiffusion coefficient, D^T , to the molecular diffusion coefficient D^M . However, for a multicomponent mixture, the thermodiffusion coefficient is more commonly used as a measure of the Soret effect.

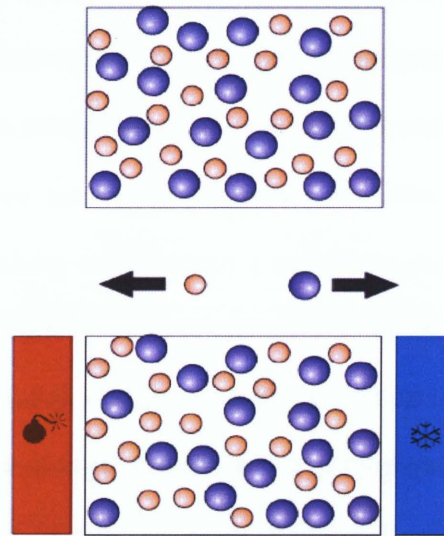


Figure 1.3: Illustration of the Soret effect. If a temperature gradient is applied to a mixture, this results in a concentration, [31].

Thermodiffusion plays a crucial role in many important processes. A particular example is thermohaline convection in oceans driven by salinity gradients associated with temperature differences [27] thermodiffusion has various technical applications, such as isotope separation in liquid and gaseous mixtures [28]; characterization and separation of polymers [29], surface coating, and crystal growth.

Thermodiffusion together with isothermal and pressure diffusion play a major role in the studies of hydrodynamic stability in fluid mixtures, migration of minerals, mass transport modeling in living matters, and the compositional variation in hydrocarbon reservoirs [30].

In low-pressure gaseous mixtures and ideal liquid mixtures, the magnitude of the thermodiffusion coefficient may be small. In contrast, in non-ideal liquid mixtures particularly, close to the critical points the thermodiffusion coefficient becomes large and strongly depends on the energetic interactions, the size and shape of the molecules and thermodynamic conditions [31].

In recent years, thermodiffusion has become a subject of extensive scientific research both theoretically and experimentally. Research on thermal-solutal convection in porous media has gained more attention; such attention has been focused on areas including underground diffusion of nuclear waste, oil reservoir analysis, tar sand extraction. Theoretical developments regarding solutal thermodiffusion have been achieved by Furry *et al.* for binary mixtures and more generally by de Groot *et al.* [32], [33] by means of irreversible process thermodynamics. A porous medium is usually defined as material that consists of a solid matrix with an interconnected void. This void also known as pores allows for the flow of one or more fluids through the material. The distribution of the pores in a natural porous medium with respect to the size and shape is irregular.

In the experimental studies for thermodiffusion, the Soret effect can be measured by using different techniques which have been divided into two different groups [34]. The first group is convection free systems and the second group of techniques uses convective coupling. In the first group, the diffusion flux in a binary mixture becomes zero ($J_i = 0$) after a steady state is achieved in the absence of convection. The resulting equations are as follows:

$$J_i = c(D^M \nabla x_i + D^T x_1(1-x_2) \nabla T) \quad (1.4)$$

$$S_T = \frac{D^T}{D^M} = \frac{\nabla x_i}{x_1(1-x_1) \nabla T} \quad (1.5)$$

where: S_T is Soret coefficient, J_i is diffusion flux of component i , x_i is mole fraction of component i , ∇x_j is a mole fraction gradient, ∇T is a temperature gradient. D^M , and D^T are the molecular and thermodiffusion coefficients, which are functions of the temperature and composition of the fluid mixture respectively.

The investigation of the thermodiffusion effect in the current model is based on the determination of D^T (thermal diffusion coefficient). In this work, D^T is determined for each species: hydrogen, water vapour and carbon dioxide at the anode side; and oxygen, water vapour and nitrogen at cathode side. Then, by adding the D^T to the Maxwell-Stefan equations, the thermodiffusion effects on the molar fraction of each species can be investigated; as exhibited and discussed in detail in chapter three.

1.5 Research Objectives

The objective of this thesis is to develop a comprehensive two-dimensional model that accounts for all important transport phenomena and electrochemical kinetics in the fuel cells. The new ingredient introduced to the fuel cell modeling study by this thesis work is the effect of thermodiffusion in the GDLs. As a result, the thermodiffusion coefficient is added to the Maxwell-Stefan equations. Detailed effects of thermodiffusion on all important transport processes of reactants and other physical phenomena will be numerically investigated. The simulation involves seven regions

of a PEM fuel cell: the anode/cathode current collector plates, two GDLs, two catalyst layers in finite thickness, and a membrane. Based on a given cell voltage, the cell current in the present model will be predicted, followed by a validation through comparison against available experimental results. The fully validated model with and without thermodiffusion will be used in a series of parametric studies to investigate the sensitivity of various operating and design parameters on fuel cell performance.

1.6 Thesis Organization

This thesis consists of four chapters and it is organized as follows:

- Chapter one presents an introduction to the fuel cell and literature review.
- Chapter two displays a model description and governing equations which are used to solve the problem. Also, the full model and the boundary conditions are described in detail. Finally, the finite element analysis is explained.
- Chapter three deals with a series of numerical experiments, including a base case study with thermodiffusion effects considered, a systematic set of parametric studies, and a validation of the numerical model through comparison of overall cell performance against experimental data obtained from other literature.
- Finally, chapter four presents the conclusions and outlooking remarks on this modeling study.

Chapter 2

Computer Model Description

A two dimensional model for a single PEM fuel cell is modeled in the y - z plane. There are five primary transport phenomena during fuel cell operation, namely, heat transfer in the solids and in the gases, fluid flow of reactant gases, convection/diffusion of different species, proton transport, and liquid water transport processes. For computation convenience, these five transport phenomena are modeled using seven computational sub-domains (from the top to the bottom as schematically shown in Figure 2.1): on the anode side, the collector plate, gas diffusion layer (GDL) and catalyst layer (CL); the ionomeric membrane; the catalyst layer, gas diffusion layer, and collector plate on the cathode side.

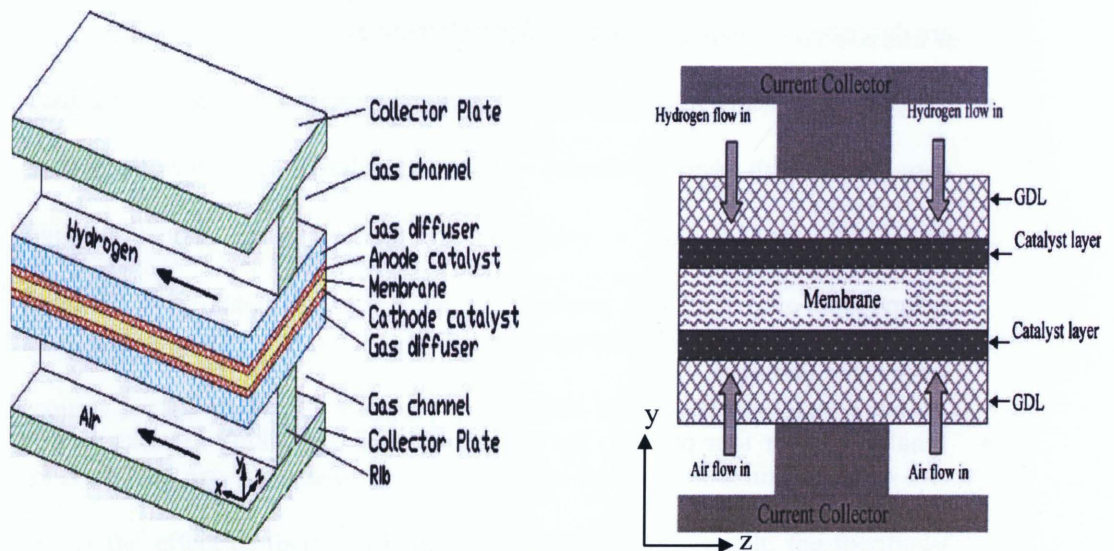


Figure 2.1: Sketch of a single PEM fuel cell configuration, [1].

In the current model, the anodic channel is supplied by hydrogen (H_2), water vapour ($H_2O_{(g)}$) and carbon dioxide (CO_2), whereas humidified air consisting of oxygen (O_2), nitrogen (N_2), and water vapor ($H_2O_{(g)}$) is fed into the cathodic channel. In the active catalyst layers on the anode and cathode sides, the hydrogen oxidation and oxygen reduction reactions occur respectively. This chapter introduces the governing equations that are used for the mathematical fuel cell models in this thesis with the boundary conditions for these equations in every subdomain. Also, the modeling parameters for this study and model validation are presented.

2.1. Model assumptions

The following assumptions will be invoked to make the model more tractable and the computation faster:

1. The transport processes are steady-state.
2. The thermodiffusion has been taken into account.
3. The flow in the gas-distribution channels is laminar.
4. The gravity effect is negligible.
5. Ohmic heating in electrodes is not neglected.
6. Though heat generation due to the electrochemical reaction is considered, the fluid properties are assumed to be independent of temperature.
7. The membrane is assumed to be impermeable for the gas-phase, for which a fairly small permeability for gases is employed to ensure nil gas concentration in the membrane.
8. The gas diffusers, the catalyst layers, and the membrane are all considered as isotropic and homogeneous porous media.

9. On the cathode side, the gaseous mixture consists of O_2 , N_2 , and $H_2O_{(g)}$ only, while on the anode side, the gaseous mixture consists of H_2 , CO_2 (due to incomplete purification of the hydrogen product), and $H_2O_{(g)}$ only, all of these gasses are assumed to be ideal gases and the gas mixture is incompressible.
10. within the gas channels, the gas diffusers, and the catalyst layers, water is purely in the form of vapour or over-saturated vapour, while water in the membrane is in the liquid phase only and exhibits a linear variation in its pressure;
11. No water phase change is taken into account within each component except that all water vapour at each interface between the catalyst layer and the membrane is entirely transformed to liquid water.

2.2. Modeling Equations in Gas Diffusion Layers (GDLs)

The gas diffusion layer (GDL) is a porous backing between the gas channel and the catalyst layer. The main functions of the diffusion layer are to distribute reactants, to remove product water to and from the area under the shoulders of the collector plates, to conduct electrons to/from the surfaces of the collector plates from/to everywhere in the catalyst layer, and to remove heat.

In the GDL, the multi-species transport processes in conjunction with heat transfer can be described using the mixture continuity equation, the Darcy equations, the energy equations, and the Maxwell-Stefan equations, (in the form developed by Curtiss and Bird [21] are used to model the transport of reactant in the electrodes).

2.2.1. Continuity and Momentum Equations

Since Darcy's law can be used to model the flow in the porous media with the pressure gradient as the driving force, Darcy's law can be used to describe the conservation of the mass and momentum for the GDLs; as, the gas channels in which the flow fields were governed by the Navier-Stokes equations, are not involved in the y-z plane model; otherwise, it is important to consider the average viscous stress terms in the outer boundary of a porous medium where the macroscopic velocity varies rapidly in space [35]. The flow governing equations are:

The continuity equation

$$\bar{\nabla} \cdot \rho \bar{V} = 0 \quad (2.1)$$

And momentum equations (Darcy's law):

$$\bar{V} = -\frac{k_p}{r^{(2)} \mu} \bar{\nabla} p \quad (2.2)$$

where k_p is the permeability of the porous electrode, μ is the viscosity of the fluid and $r^{(2)}$ is a coefficient describing the effect of the porosity of the medium to the viscous force. Eq. (2.2) turns into the Brinkman's equations, if $r^{(2)} = 1$. We can get $r^{(2)}$ from [35]:

$$r^{(2)} = 2.25 \frac{(1 - \varepsilon_g)^2}{\varepsilon_g^2} \quad (2.3)$$

Darcy's equation is proposed empirically to describe the slow seepage of fluids through granular media by homogenization of the porous and fluid media into one single medium, so that a detailed geometric description of the pore structure is not required [36].

2.2.2. Mass Transport Equations

In a binary diffusion, the movement of any species is proportional to the negative of the concentration gradient of this species. In multicomponent diffusion, other interesting things can arise such that (i) the species can move against its concentration gradient which is known as reversed diffusion; (ii) the species can move in the absence of its concentration gradient, which is called osmotic diffusion; and (iii) the species may not diffuse though its concentration gradient, which is called nonzero diffusion.

Maxwell-Stefan equations are shown to be a very good approximation for multicomponent diffusion in gases at low density [37], [38]. Curtiss and Bird revised the Maxwell-Stefan equations by using different diffusivities to validate the equations for dense gases, liquids and polymers. Unlike the conventional one, their formulation incorporates the pressure dependence and the temperature dependence of the concentration gradient of the species. The formulation is adopted in this study, and briefly explained as follows:

The mass balance for each species, except one, in a solution is given by the general transport equation:

$$\frac{\partial}{\partial t}(\rho w_i) + \nabla \cdot (j_i + \rho w_i u) = R_i \quad (2.4)$$

where w_i is the mass fraction of the species and R_i is the reaction rate. The second term in this equation is the combined mass flux consisting of molecular mass flux vector j_i and the convective mass flux vector with the velocity vector u . j_i describes the diffusion-driven transport, which is the property investigated by Curtiss and Bird. They derived their description of the molecular mass flux from Jaumann's entropy-balance equation [39] and were able to describe diffusion transport as a function of

temperature and a diffusion driving force d_j . Hence, with the thermodynamics of irreversible processes, j_i is defined as:

$$j_i = -D_i^T \nabla(\ln T) - \rho w_i \sum_{j=1}^N D_{ij} d_j \quad (i=1, 2, \dots, N) \quad (2.5)$$

where D^T is the thermal diffusion coefficient, T is the temperature, D_{ij} are the symmetric diffusivities proposed by Curtiss, and d_j is the diffusion driving force for the species j , which is defined as:

$$d_i = \frac{1}{cRT} \left(\nabla p_i - w_i \nabla p - \rho w_i g_i + w_i \sum_{j=1}^N \rho w_j g_j \right) \quad (2.6)$$

where c is the concentration of the mixture, R is the universal gas constant and g_{ij} is the force per unit mass acting on the i^{th} species. The first two terms on the right side of Eq. (2.6) describe the effects of the intermolecular forces, and the last two terms describe the effects of the external forces. If the only external force is the gravity, the last two terms cancel each other. Noting that from the ideal gas law $p = cRT$ and the mole fraction of the species i is

$$x_i = \frac{p_i}{p} \quad (2.7)$$

Eq. (2.6) can then be written as:

$$d_i = \left(\nabla x_i + (x_i - w_i) \frac{\nabla p}{p} - \rho w_i g_i + w_i \sum_{j=1}^N \rho w_j g_j \right) \quad (2.8)$$

With the assumptions that the transport processes are steady-state and there is no external force acting on the species apart from the gravity, by substituting Eqs. (2.5) and (2.8) into Eq. (2.4), the resulting mass balance in the mass fractions reads:

$$\bar{\nabla} \cdot \left[\rho w_i \bar{V} - \rho w_i \sum_{j=1}^n D_{ij} \left\{ \bar{\nabla} x_j + (x_j - w_j) \frac{\bar{\nabla} p}{p} \right\} - D_i^T \frac{\bar{\nabla} T}{T} \right] = R_i \quad (2.9)$$

where, on the anode side, the subscripts i and j are applied to denote hydrogen, water

vapour, carbon dioxide; while, on the cathode side, i and j are applied to denote oxygen, water vapor, and nitrogen; x_i is the mole fraction of the component i ; N_i is the molar flux of the component i ; c stands for the concentration; and D_{ij} represents the binary diffusivity of species i and j . On the cathode side, the ternary mixture of three species is viewed in three species pairs: $O_2 - N_2$, $N_2 - H_2O_{(g)}$, and $O_2 - H_2O_{(g)}$, while on the anode sides, the three species pairs are: $H_2 - CO_2$, $CO_2 - H_2O_{(g)}$, and $H_2O_{(g)} - H_2$. The binary diffusivities D_{ij}^0 are usually obtained by experiment at the atmospheric pressure p_{atm} and reference temperature T_0 ; according to [16], D_{ij}^0 can then be scaled to the operating temperature and pressure as follows:

$$D_{ij} = D_{ij}^0(T_0, p_0) \frac{p_0}{p} \left(\frac{T}{T_0} \right)^{1.5} \quad (2.10)$$

Due to the porous nature of the gas diffusers, the binary diffusivity correction is taken for the porous media. The resulting species equations become:

$$\bar{\nabla} \cdot \left[\rho w_i \bar{V} - \rho w_i \sum_{j=1}^n D_{ij}^{eff} \left\{ \bar{\nabla} x_j + (x_j - w_j) \frac{\bar{\nabla} p}{p} \right\} - D_i^T \frac{\bar{\nabla} T}{T} \right] = 0 \quad (2.11)$$

where the binary diffusivities D_{ij} are corrected for the flow in porous media by using the so-called *Bruggemann* correction formula [40]:

$$D_{ij}^{eff} = D_{ij} \varepsilon_g^{1.5} \quad (2.12)$$

Note the right hand side of Eq. (2.11) vanishes because there is no reaction rate R_i in GDL. In the Eq. (2.11), D^T denotes the multicomponent thermodiffusion coefficient and is calculated with the following equation [41]:

$$D_i^T = -2.59 \cdot 10^{-7} \cdot T_f^{0.659} \left[\frac{\sum_{i=1}^n M_i^{0.511} \cdot w_i}{\sum_{i=1}^n M_i^{0.511} \cdot w_i} - x_i \right] \cdot \left(\frac{\sum_{i=1}^n M_i^{0.511} \cdot w_i}{\sum_{i=1}^n M_i^{0.489} \cdot w_i} \right) \quad (2.13)$$

It is possible to express the molar fraction x_i in the term of mass fraction ω_i by [13]:

$$x_i = \frac{\frac{\omega_i}{M_i}}{\sum_{j=1}^n \frac{\omega_j}{M_j}} \quad (2.14)$$

the above equation can also be written as:

$$\omega_i = \frac{x_i M_i}{\sum_{j=1}^n x_j M_j} = \frac{x_i M_i}{M} \quad (2.15)$$

where M stands for the total mole mass of the mixture calculated using:

$$M = \sum_{i=1}^n M_i x_i \quad (2.16)$$

and M_i indicates the mole mass of the species i . Assumption 7 implies the applicability of *the state equation*, which relates density, temperature and pressure. That is, for each species i contained in the ternary system, such as the mixture of O_2 , N_2 and $H_2O_{(g)}$ at the cathode side and the mixture of H_2 , CO_2 and $H_2O_{(g)}$ at the anode side, the following relationship holds:

$$\rho_i = M_i \frac{P_g}{RT_g} \quad (2.17)$$

Though, theoretically Eq. (2.11) can be used for each species in the gas mixture, the mass and molar fractions for CO_2 on the anode side and N_2 on the cathode side are practically calculated by using:

$$\omega_n = 1 - \sum_{i=1}^{n-1} \omega_i \quad (2.18)$$

$$x_n = 1 - \sum_{i=1}^{n-1} x_i \quad (2.19)$$

which ensures the conservation of mass on both sides. Therefore, the Maxwell-Stefan diffusion and convection equation applies only to 2 species out of the 3 species on one electrode side. The final species is solved through the fact that:

$$\sum_{i=1}^n w_i = 1 \quad (2.20)$$

2.2.3. Solid-Phase Potential Equations

There is no electron produced in gas diffusion layers, as the GDL works as a bridge between the current-collecting land and catalyst layer to provide electron lateral conduction. The electron current density i_e in the gas diffusers satisfies:

$$\bar{\nabla} \cdot \bar{i}_e = 0 \quad (2.21)$$

where the electron current density i_e can be described by:

$$\bar{i}_e = -\sigma_{GDL}^e \bar{\nabla} \phi_s \quad (2.22)$$

where σ_{GDL}^e is the electrical conductivity of the gas diffuser. Conductivity is the inverse of electrical resistivity and has the SI units of Siemens per meter (S/m).

By substituting Eq. (2.22) into Eq. (2.21) the solid-phase potential can be obtained by solving:

$$\bar{\nabla} \cdot (-\sigma_{GDL}^e \bar{\nabla} \phi_s) = 0 \quad (2.23)$$

2.2.4. Energy equation

Energy balance is important since most chemical reactions either require or produce heat, which in turn affects both the reactions themselves and other physical processes connected to the system. By overall averaging of the microscopic energy equations in both fluid and solid phase, the effective conductivity becomes a function of the fluid phase and solid matrix conductivities, which satisfies:

$$k_{eff} = -2k_{gr} + \frac{1}{\frac{\epsilon_g}{2k_{gr} + k_{gas}} + \frac{1 - \epsilon_g}{3k_{gr}}} \quad (2.24)$$

where k_{gas} and k_{gr} are the thermal conductivities of the gas mixture and of the graphite solid matrix, respectively. Because there is electron current in the gas diffusers, the energy equation for the gas diffusers can be written as:

$$\rho c_p (\bar{V} \cdot \bar{\nabla} T) = k_{eff} \Delta T + \frac{i_e^2}{\sigma_{GDL}^e} \quad (2.25)$$

Note the last term represents the heat source term produced as a result of the ohmic heating of electron current i_e .

2.3. Modeling Equations in Catalyst Layers

2.3.1 Flow Model: Darcy's law

The catalyst layers usually consist of platinum, carbon, membrane material, and Teflon. Since catalyst layers are made highly porous and the components neighboring the catalyst are the porous electrode and membrane, the velocity variation taking place at the interfaces within the MEA is fairly small. As the sole driving force, Darcy's law can be applied to model the flow in the porous catalysts.

Darcy's law states that the velocity vector is determined by the pressure gradient, $\bar{\nabla} p$, the fluid viscosity, μ , and the structure of the porous media, resulting in the following equation:

$$\bar{V} = -\frac{k_h}{r^{(2)} \mu} \bar{\nabla} p \quad (2.26)$$

Gagan [35] estimated $r^{(2)}$ in the catalyst layer by using:

$$r^{(2)} = 2.25 \frac{(1 - \varepsilon_{ct})^2}{\varepsilon_{ct}^2} \quad (2.27)$$

where the effective porosity of the catalyst layer ε_{ct} can be calculated by:

$$\varepsilon_{ct} = \varepsilon_m \cdot \theta_{mc} \quad (2.28)$$

where ε_m and θ_{mc} denote the porosity of the membrane and the volume fraction of the membrane in the catalyst layer, respectively.

2.3.2. Electrochemical Modeling Equations

Transport phenomena in the catalyst layers are complicated because of the electrochemical reactions. The electrochemical reactions can be modeled by the Butler-Volmer equations [7]:

$$j_a = (aj_0^{ref})_a \left(\frac{c_{H_2}}{c_{H_2,ref}} \right)^{1/2} \left[\exp\left(\frac{\alpha_a^a F}{RT} \eta_a \right) - \exp\left(-\frac{\alpha_c^e F}{RT} \eta_a \right) \right] \quad (2.29)$$

$$j_c = (aj_0^{ref})_c \left(\frac{c_{O_2}}{c_{O_2,ref}} \right) \left[\exp\left(\frac{\alpha_a^c F}{RT} \eta_c \right) - \exp\left(-\frac{\alpha_c^c F}{RT} \eta_c \right) \right] \quad (2.30)$$

where j_a and j_c are the exchange current densities of the anode and cathode, respectively; a the catalyst surface area per unit volume; j_0^{ref} the reference exchange current densities; c_{H_2} and c_{O_2} the hydrogen and oxygen concentrations, respectively; α_a^a and α_c^e the anodic transfer coefficients at the anode and cathode, respectively; α_a^c and α_c^c the cathodic transfer coefficients at the anode and cathode, respectively; F Faraday's constant; $c_{H_2,ref}$ and $c_{O_2,ref}$ the corresponding reference concentrations, respectively; η_a and η_c the activation overpotentials at the anode and cathode, respectively; the kinetic expressions in Eqs. (1.1) and (1.2) represent the hydrogen oxidation reaction (HOR) in the anode catalyst layer and oxygen reduction reaction (ORR) in the cathode catalyst layer, respectively.

The surface overpotential for an electrochemical reaction, η is considered the driving

force for an electrochemical reaction, and can be described as:

$$\begin{cases} \eta_a = \phi_s - \phi_p & \text{at anode} \\ \eta_c = \phi_s - \phi_p - E_0 & \text{at cathode} \end{cases} \quad (2.31)$$

where ϕ_s is the solid-phase potential, ϕ_p is membrane-phase potential, and E_0 is the thermodynamic open circuit potential for overall reaction, which is expressed by the *Nernst* equation [7] as a function of the reactant and product concentrations at the interface:

$$E_0 = 1.23 - 0.9 \times 10^{-3} (T - 298) + 2.3 \frac{RT}{4F} \log(p_{H_2}^2 p_{O_2}) \quad (2.32)$$

Beattie *et al.* [42] tabulated the experiential results for the open circuit potential, which are fitted into a linear function of temperature as proposed:

$$E_0 = 0.0025T + 0.2329 \quad (2.33)$$

2.3. 3. Mass Transport Equations

The mass transport equation used in the catalyst layers takes the exchange current densities over both anodic and cathodic catalyst layers into account:

$$\bar{\nabla} \cdot \left[-\rho \omega_i \sum_{j=1}^n D_{ij}^{eff} \left\{ \bar{\nabla} x_j + (x_j - \omega_j) \frac{\bar{\nabla} p}{p} \right\} - D_i^T \frac{\bar{\nabla} T}{T} \right] = -\rho \bar{V} \cdot \bar{\nabla} \omega_i + S_k \quad (2.34)$$

where S_k is the source/sink term for species k . As seen from the chemical reaction given by Eqs. (1.1) and (1.2), in order to produce one electron with the charge of one Coulomb, $\frac{1}{2}$ mole of hydrogen from the anode side and $\frac{1}{4}$ mole oxygen from the cathode side are needed, and $\frac{1}{2}$ mole of water will be produced at the cathode side. Therefore, at the anode catalyst layer, hydrogen is consumed to produce electrons and protons. Hydrogen is oxidized with local sink (source) terms for hydrogen and water:

$$S_{H_2} = -\frac{j_a}{2F} M_{H_2} \quad (2.35)$$

$$S_{H_2O} = 0 \quad (2.36)$$

where M_{H_2} is the molecular weight of hydrogen, and no water is produced or depleted in the anodic catalyst layer as shows in Eq. (2.36) ; alternatively, the mass generation source terms at the cathode catalyst layer are defined as:

$$S_{O_2} = \frac{j_c}{4F} M_{O_2} \quad (2.37)$$

$$S_{H_2O} = -\frac{j_c}{2F} M_{H_2O} \quad (2.38)$$

where M_{O_2} and M_{H_2O} are the molecular weights of oxygen and water, respectively. Also, j_c and j_a are the transfer current density at the cathode and anode, which represent the reaction rates. The value j_a is positive and j_c is negative, according to Eqs (2.29) and (2.30), respectively.

2.3.4. Energy Equations

The electrochemical reaction taking place in the anode and cathode catalyst layers lead to migration of the electrons and protons through the layers. Thus, the energy equation can be expressed as:

$$\rho c_p (\vec{V} \cdot \vec{\nabla} T) = k_{ct,eff} \Delta T + \frac{i_p^2}{\sigma_{ct}^m} + \frac{i_e^2}{\sigma_{ct}^e} + \begin{cases} \eta_a \cdot j_a & \text{at anode} \\ \eta_c \cdot j_c & \text{at cathode} \end{cases} \quad (2.39)$$

where σ_{ct}^m and σ_{ct}^e are proton and electronic conductivity within catalyst layers, respectively, while i_e and i_p are electron and proton current density, respectively. On the right hand side of the above equation, the second and third terms describe the ohmic heating of both proton current i_p and electron current i_e within catalyst layers; and the last term represents the heat generation or absorption because of electrochemical reaction at the catalyst.

2.3.5. Solid-phase and membrane-phase potential equations

Although the catalyst layers are relatively small, they are the heart of a fuel cell, where fuel and oxidant react electrochemically to produce electrical energy. In the anodic catalyst layer, hydrogen-rich fuel fed to the anode side diffuses through the porous gas diffusion layer (GDL); the hydrogen splits into hydrogen protons and electrons. Electrons pass through an external circuit to the cathode, thus providing electrical power, while the protons transport through the membrane to the cathode. In the cathodic catalyst layer, oxygen combines with protons and electrons to produce water. Figure 2.2 shows the transportation paths for protons and electrons forming a closed electrical circuit.

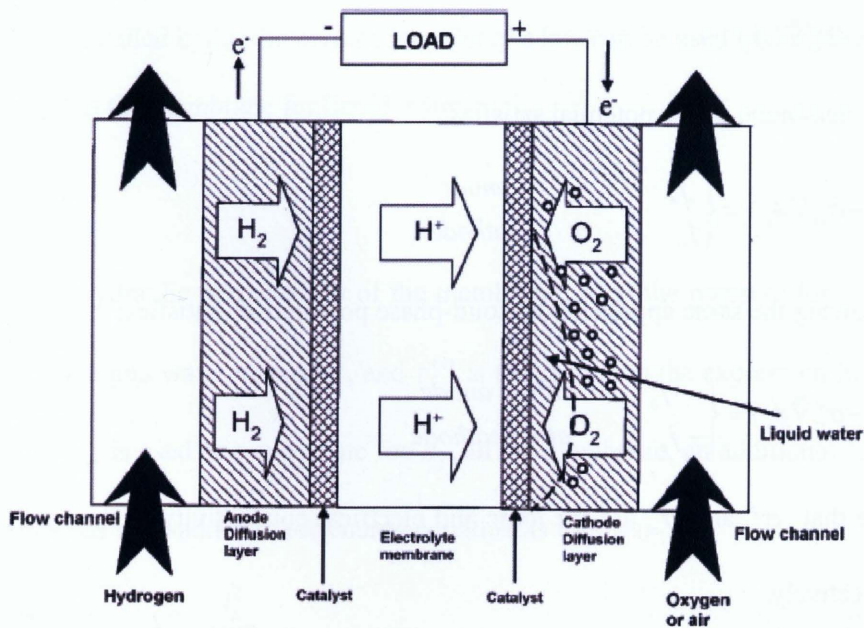


Figure 2.2: Transport paths of protons and electrons within a PEM fuel cell, [52].

In the anode catalyst layer, and cathode catalyst layer, the proton current density

i_p and the electron current density i_e satisfy:

$$\bar{\nabla} \cdot \bar{i}_p = \begin{cases} j_a & \text{at anode} \\ j_c & \text{at cathode} \end{cases} \quad (2.40)$$

$$\bar{\nabla} \cdot \bar{i}_e = \begin{cases} -j_a & \text{at anode} \\ -j_c & \text{at cathode} \end{cases} \quad (2.41)$$

Generally, the current density conservation law follows:

$$\bar{\nabla} \cdot \bar{i}_p + \bar{\nabla} \cdot \bar{i}_e = 0 \quad (2.42)$$

This means:

$$\bar{i}_p + \bar{i}_e = \text{constant} \quad (2.43)$$

That leads to the membrane-phase potential ϕ_p and the proton current density i_p being interrelated by:

$$\bar{i}_p = -\sigma_{ct}^p \bar{\nabla} \cdot \phi_p \quad (2.44)$$

The membrane-phase potential satisfies:

$$\bar{\nabla} \cdot (-\sigma_{ct}^p \bar{\nabla} \phi_p) = \begin{cases} j_a & \text{at anode} \\ j_c & \text{at cathode} \end{cases} \quad (2.45)$$

Following the same approach, the solid-phase potential ϕ_s satisfies:

$$\bar{\nabla} \cdot (-\sigma_{ct}^e \bar{\nabla} \phi_s) = \begin{cases} -j_a & \text{at anode} \\ -j_c & \text{at cathode} \end{cases} \quad (2.46)$$

Note that σ_{ct}^p and σ_{ct}^e are the ionic and electrical conductivity of the catalyst layers, respectively.

2.4. Modeling Equations in Membrane

The major function of the membrane is to transfer protons from anode to cathode. As the protonic conductivity of the membrane depends robustly on its water content, the

polymer electrolyte must be kept hydrated during operation. On the other hand, flooding of the porous electrodes and GDL should be avoided so that reactants can be transported effectively to the reaction sites in the catalyst layer. In the membrane, water is assumed to exist in its liquid phase while the reactant gases are considered impermeable. Properties of interest in the membrane are the liquid water flux, the electrical potential distribution, and temperature distribution, which have effects on the ionic conductivity. The governing equations in the membrane are the same in the catalyst layer, but without any chemical reaction.

2.4.1. Darcy's Law and Energy Equations

The membrane is a porous medium and water can migrate through it by pressure difference that is called hydraulic permeation. Darcy's law can be used to describe the water transport in the membrane for liquid water:

$$\bar{V} = -\frac{k_h}{r^{(2)}\mu_l}\bar{\nabla}p_l \quad (2.47)$$

where k_h is the hydraulic permeability of the membrane, p_l is the pressure for liquid water, μ_l is the liquid water viscosity, and $r^{(2)}$ is related to the expression in Eq. (2.3) in which ε_m is used as a substitute for ε_g . In the membrane, an additional Joule heating source has been added to the energy equation as follows:

$$\rho c_p (\bar{V} \cdot \bar{\nabla} T) = k_{m,eff} \Delta T + \frac{i_p^2}{\sigma_m^p} \quad (2.48)$$

where σ_m^p appears in the Joule heating source term representing the ionic conductivity in the membrane. It depends on many factors, for instance, temperature, methods of pretreatment, the type of membrane and its equivalent weight, as well as other

external variables and the amount of water uptake, etc. The effective thermal conductivity in the membrane $k_{m,eff}$ satisfies:

$$k_{m,eff} = -2k_{m,dry} + \frac{1}{\frac{\varepsilon_m}{2k_{m,dry} + k_{w,l}} + \frac{1-\varepsilon_m}{3k_{m,dry}}} \quad (2.49)$$

where $k_{w,l}$ is the thermal conductivity of liquid water, ε_m is the membrane porosity, and $k_{m,dry}$ is the thermal conductivity of a dry membrane.

2.4.2. Water and Proton Transport Model

The transport models of water and proton have been investigated in this study. Particularly, the effect of membrane swelling on water content and potential loss within the membrane is examined. The permeability of the membrane to hydrogen, oxygen, nitrogen and carbon dioxide is low and can be neglected as stated in assumption 7. Thus, only water and protons are transported in the membrane, where both follow the principle of mass conservation. While the exact and complete mechanism of water transport in the membrane is still under investigation, an updated model formulated by Cao *et al.* [13], has been used here to allow quantitative assessment of fuel cell operation with a membrane under the partial hydration condition.

Conservation equations for liquid water and protons satisfy:

$$\bar{\nabla} \cdot \bar{N}_w = 0 \quad (2.50)$$

and

$$\bar{\nabla} \cdot \bar{N}_p = 0 \quad (2.51)$$

where \bar{N}_w and \bar{N}_p are the molar flux of water and that of protons, respectively. And the positive values for \bar{N}_w or \bar{N}_p indicate net water flux or proton flux from the anode to the cathode, while negative values means, a net flux from the cathode to the anode side.

2.4.2.1. Water Transport

There are three mechanisms of water transport in the membrane: electro osmotic drag, diffusion, and hydraulic permeation, which are induced separately by the moving protons, the water concentration difference, and the pressure difference between the two sides of the membrane. A good water management procedure is to balance the three water fluxes so that the membrane is kept well-hydrated while avoiding flooding, as shown in Figure 2.3.

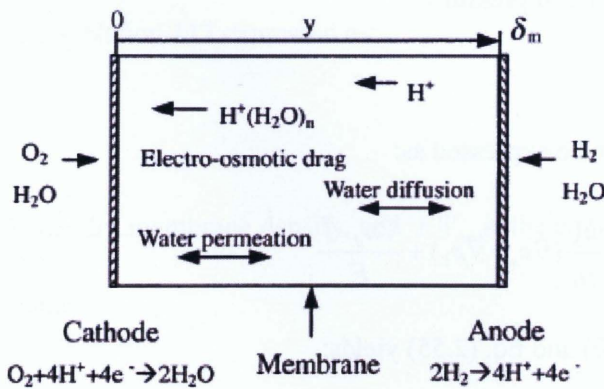


Figure 2.3: Schematic of water transport phenomena in a proton exchange membrane [4].

The net water flux through the membrane is the sum of these three water fluxes and is expressed by the following equation:

$$\bar{N}_w = -D_w \bar{\nabla} c_w - c_w \varepsilon_w^m \frac{k_h}{\mu_l} \bar{\nabla} p_l + \frac{n_d \bar{i}_p}{F} \quad (2.52)$$

where N_w is the molar flux of water, c_w denotes the molar concentration of water, ε_w^m the volume fraction of water in the membrane, D_w the diffusion coefficient, k_h the hydraulic permeability of the membrane, μ_l the liquid water viscosity, n_d the electro-osmotic drag coefficient, F Faraday's constant, p_l the water pressure, and \bar{i}_p is the proton current density that equals the local current density \bar{i} in the membrane, as there is no electron transport in the membrane. This equation accounts for back diffusion processes induced by the water concentration gradient, which provides the model with improved capability of predicting humidification schemes.

Taking into account the current density conservation:

$$\bar{\nabla} \cdot \bar{i} = 0 \quad (2.53)$$

along with the linear profile of pressure:

$$\nabla^2 p_l = 0 \quad (2.54)$$

the divergence of \bar{N}_w can be expressed as:

$$\bar{\nabla} \cdot \bar{N}_w = -D_w \nabla^2 c_w - \varepsilon_w^m \frac{k_h}{\mu_l} (\bar{\nabla} c_w \cdot \bar{\nabla} p_l) + \frac{\bar{\nabla} n_d \cdot \bar{i}}{F} \quad (2.55)$$

Combination of Eq. (2.50) and Eq. (2.55) yields:

$$-D_w \nabla^2 c_w - \varepsilon_w^m \frac{k_h}{\mu_l} (\bar{\nabla} c_w \cdot \bar{\nabla} p_l) + \frac{\bar{\nabla} n_d \cdot \bar{i}}{F} = 0 \quad (2.56)$$

Based on the experiments using Nafion117, Springer et al. [5] proposed a simple linear relationship between the electro-osmotic drag coefficient, n_d and the membrane water content:

$$n_d = \frac{2.5}{22} \lambda \quad (2.57)$$

where λ is the hydration index, which is defined as the number of moles of water per equivalent sulfonic acid group, SO_3^- , in the membrane; the numeric values 2.5 and 22 correspond to the number of water molecules dragged per migrating H^+ ion and the possible maximum hydration index, respectively.

Springer *et al* [5] expanded the dry membrane thickness dimensions by the factor $(1 + f\lambda)$ to account for membrane swelling, and presented an empirical formula relating c_w to λ as follows:

$$c_w = \frac{e\lambda}{f\lambda + 1} \quad (2.58)$$

where f is the membrane swelling coefficient experimentally determined through the measured thicknesses of the dry and fully hydrated Nafion 117 membranes, and e is a constant ratio for Nafion 117 expressed as:

$$e = \frac{\rho_m^{dry}}{EW_m} \quad (2.59)$$

where ρ_m^{dry} is the dry membrane density, and EW_m is the equivalent molecular weight of the membrane.

Since, the membrane water diffusivity is related to the temperature and water content of the membrane, its formula of empirical nature is satisfied by [5]:

$$D_w = 10^{-6} \exp \left[2416 \left(\frac{1}{303} - \frac{1}{T} \right) \right] (2.563 - 0.33\lambda + 0.0264\lambda^2 - 0.000671\lambda^3) \quad (2.60)$$

Re-arranging Eq. (2.58) leads to:

$$\lambda = \frac{c_w}{e - fc_w} \quad (2.61)$$

The electro-osmotic drag coefficient n_d for Nafion117 expressed in Eq. (2.57) can now be re-written as a function of water concentration:

$$n_d = \frac{2.5}{22} \frac{c_w}{e - fc_w} \quad (2.62)$$

Substituting Eq. (2.62) into Eq. (2.56), the water transport equation can be expressed as:

$$-D_w \nabla^2 c_w - \varepsilon_w^m \frac{k_h}{\mu_l} (\bar{\nabla} c_w \cdot \bar{\nabla} p_l) + \frac{5}{44} \frac{e}{F(e - fc_w)^2} (\bar{\nabla} c_w \cdot \bar{i}) = 0 \quad (2.63)$$

which is a complete mathematical description of water concentration distribution in the membrane. Eq. (2.63) can be viewed as a nonlinear partial differential equation of c_w with the known pressure profile p_l and current density \bar{i} in the membrane,

2.4.2.2. Proton Transport

The *Nernst-Planck* equation can be used to determine the flux of protons through the membrane, representing that the migration, diffusion, and convection of the dissolved protons cause the net molar flux of protons:

$$\bar{N}_p = -Z_p \frac{F}{RT} D_p c_p \bar{\nabla} \phi_p - D_p \bar{\nabla} c_p + c_p \bar{V}_l \quad (2.64)$$

where D_p is the diffusion coefficient, c_p is the molar concentration of protons, Z_p is the charge number of ion, ϕ_p is the electric potential, i.e., membrane-phase potential, and V_l is the convective velocity of the liquid water.

By using *Schliögl* equation [43], [44], the velocity of liquid water in the pores of the membrane can be estimated:

$$\bar{V}_l = \varepsilon_w^m \left(\frac{k_\phi}{\mu_l} Z_f c_f F \bar{\nabla} \phi - \frac{k_h}{\mu_l} \bar{\nabla} p_l \right) \quad (2.65)$$

where Z_f is the charge number of the fixed charges, k_ϕ and k_h are the electric and hydraulic permeabilities of the membrane, respectively, and c_f is the fixed-charged concentration.

As the electric current results from the flux of charge species, the current density in the membrane can be expressed as:

$$\bar{i} = F \sum Z_j \bar{N}_j = F \bar{N}_p \quad (2.66)$$

where \bar{N}_j is the molar flux of ions, Z_j is the charge number of the charged mobile ion of species j , and $Z_j = 1$ for the sole mobile ions, which are the hydrogen ions in this situation. Thus, Eq. (2.66) becomes:

$$\bar{N}_p = \frac{\bar{i}}{F} \quad (2.67)$$

The membrane ionic conductivity is commonly defined as:

$$\sigma_m^p = \frac{F^2}{RT} \sum Z_j^2 D_j c_j \quad (2.68)$$

The electro-neutrality condition signifies that no net charge should exist in the membrane:

$$Z_f c_f + \sum Z_j c_j = 0 \quad (2.69)$$

Since only a proton charged mobile ion in the membrane (for H^+) and $Z_p = 1$, thus Eq. (2.68) can be reduced to:

$$\sigma_m^p = \frac{F^2}{RT} D_p c_p \quad (2.70)$$

and, Eq. (2.69) becomes:

$$Z_f c_f = -c_p \quad (2.71)$$

Substituting Eq. (2.71) into Eq. (2.64) and (2.65) results in:

$$\bar{N}_p = -\frac{F}{RT} D_p c_p \bar{\nabla} \phi_p - D_p \bar{\nabla} c_p + c_p \bar{V}_l \quad (2.72)$$

and

$$\bar{V}_l = \varepsilon_w^m \left(\frac{k_\phi}{\mu_l} c_p F \bar{\nabla} \phi - \frac{k_h}{\mu_l} \bar{\nabla} p_l \right) \quad (2.73)$$

Combining Eq. (2.72) and (2.73) with the divergence of Eq. (2.51) gives:

$$-\Delta \phi_p = -\frac{1}{\sigma_m^p} [\bar{\nabla}(\ln c_p) \cdot \bar{i}] + \frac{RT}{F} \bar{\nabla} \cdot [\bar{\nabla}(\ln c_p)] c_p \quad (2.74)$$

where c_p is a function of hydration. Unlike the unrealistic assumption of a constant c_p as employed in many other previous studies, the concentration of protons is now allowed to vary in response to the swelling or drying of the membrane due to the change of internal liquid water. Since in the membrane the hydration index, λ , is defined as the number of moles of water per equivalent sulfonic acid group, for Nafion 117, the proton concentration can be expressed as:

$$c_p = \frac{c_w}{\lambda} \quad (2.75)$$

Substituting Eq. (2.58) into (2.75) leads to:

$$c_p = \frac{e}{f\lambda + 1} \quad (2.76)$$

Substitution Eq. (2.61) in Eq. (2.76) leads to:

$$c_p = e - fc_w \quad (2.77)$$

Invoking Eq. (2.77) into Eq. (2.74), the electrical membrane-phase potential can be expressed in terms of water concentration c_w :

$$\begin{aligned}
-\Delta\phi_p = & -\frac{1}{\sigma_m^p} \frac{f}{e - fc_w} (\bar{\nabla}c_w \cdot \bar{i}) - \frac{RTe}{F} \frac{f}{e - fc_w} \Delta c_w \\
& - \frac{RT}{F} \left(\frac{f}{e - fc_w} \right)^2 (\bar{\nabla}c_w \cdot \bar{\nabla}c_w)
\end{aligned} \tag{2.78}$$

In order to eliminate Δc_w , i.e. $\nabla^2 c_w$, Eq. (2.63) is substituted into Eq. (2.78) and the electric potential equation in the membrane accounting for the swelling effect is finally written as:

$$\begin{aligned}
-\Delta\phi_p = & -\frac{f}{e - fc_w} \left(\frac{1}{\sigma_m^p} - \frac{5}{44} \frac{RTe}{D_w F^2 (e - fc_w)^2} \right) (\bar{\nabla}c_w \cdot \bar{i}) \\
& + \frac{RT}{F} \frac{f}{e - fc_w} \frac{\varepsilon_w^m}{D_w \mu_l} (\bar{\nabla}c_w \cdot \bar{\nabla}p_l) \\
& - \frac{RT}{F} \left(\frac{f}{e - fc_w} \right)^2 (\bar{\nabla}c_w \cdot \bar{\nabla}c_w)
\end{aligned} \tag{2.79}$$

The ionic conductivity of a Nafion117 proton exchange membrane is expressed by Springe *et al.* [5] as:

$$\sigma_m^{ref} = 0.5139\lambda - 0.326 \quad \text{if } \lambda \geq 1 \tag{2.80}$$

where σ_m^{ref} is the reference ionic conductivity measured at 303K. The reference ionic conductivity is assumed constant for the values of membrane water content, $\lambda < 1$. At other temperatures, it is corrected to be a function of operating temperature T [5]:

$$\sigma_m^p = \sigma_m^{ref} \exp \left[1268 \left(\frac{1}{303} - \frac{1}{T} \right) \right] \tag{2.81}$$

2.5. Collector plates

Since the bipolar plates serve to transfer the electrons and separate different cells, the solid-phase potential equations accounting for the electron transport in the current plates have to be added to the simulation model:

$$\bar{\nabla} \cdot (-\sigma_{plate}^e \bar{\nabla}\phi_s) = 0 \tag{2.82}$$

where σ_{plate}^e is the electrical conductivity of current plates. In the present model, the value of σ_{plate}^e is assumed to be 20000 S/m [45].

2.6. Boundary Conditions

Corresponding to the equation systems, in practice, some subdomains may be grouped to be subjected to an identical governing equation. For example, the oxygen is transported in the cathode gas diffusion layer (GDL), and catalyst layer (CL); then, the Maxwell-Stefan equation for the oxygen transport applies to both subdomains. Accordingly, the boundary conditions for the mass fraction of oxygen are required only at the border of the grouped subdomains, while no specification of interfacial conditions is required between neighboring subdomains in the group.

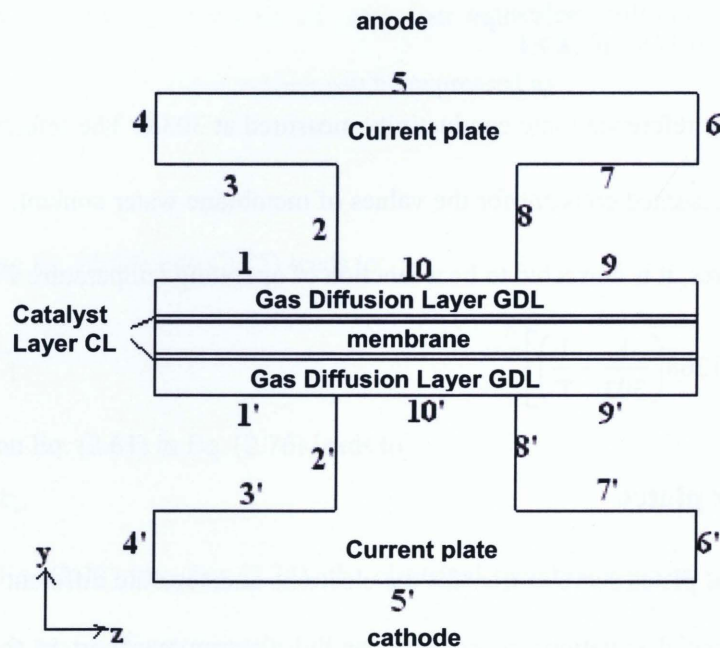


Figure 2.4: Schematic diagram of computation model of a PEM fuel cell in y-z plane.

For the sake of convenience, all boundaries in the model are named as #1, #1', etc. In the y - z plane, additional components, the current plate/current collectors, are involved in the two-dimensional model, while the anode/cathode gas channels may be extracted from the computational domains since the cross flow within the channels is insignificant. Hence, in the two-dimensional model of a PEM fuel cell in the y - z plane, there are seven computational subdomains including the anode/cathode current plates, GDLs, catalyst layers, and membrane, as shown in Figure 2.4 which schematizes all boundaries of a 2D PEM fuel cell model in the y - z plane.

2.6.1 Darcy's Law

Since gas diffusion layers (GDLs), catalyst layers (CLs) and the membrane domains are porous structure, Darcy's law can be apply within these entire domains. The pressure boundary values are prescribed at the operating pressures for the interfaces between the gas channels and GDLs for both anode and cathode sides. That is:

$$\text{For Boundaries \#1, \#9:} \quad p = p_a \quad (2.83)$$

$$\text{For Boundaries \#1', \#9',} \quad p = p_c \quad (2.84)$$

where p is the local pressure, p_a and p_c are the operating pressures at the anode and cathode sides, respectively. For both anode and cathode sides, insulation condition are specified at the interfaces between the GDLs and collector plate as well as at the inlet and outlet for both GDLs and catalyst layers CLs.

2.6.2 Species Equations

To describe the species transport in the gas diffusion layers (GDLs) and catalyst layers; the Maxwell-Stephan equations are applied. At the anodic and cathodic interfaces between the gas channels and GDLs, i.e., boundaries #1,#1', #9, and #9' (as shown in Figure 2.5), each of the mass fractions of H_2 , O_2 is prescribed using a constant inlet value. The mass fractions of water vapor at the anode and cathode sides can determine as follow respectively:

$$\omega_{H_2O,a} = RH \frac{p^{sat} M_{H_2O}}{p_a M} \quad (2.85)$$

$$\omega_{H_2O,c} = RH \frac{p^{sat} M_{H_2O}}{p_c M} \quad (2.86)$$

where RH is the relative humidity, p_a and p_c are the operating pressures at the anode and cathode sides; p^{sat} is the saturated water partial pressure calculated using the following empirical equation [5]:

$$\log_{10} p^{sat} = -2.1794 + 0.02953T - 9.1837 \times 10^{-5} T^2 + 1.4454 \times 10^{-7} T^3 \quad (2.87)$$

A homogeneous Neumann boundary condition was specified for the oxygen mass fraction equation, a boundary condition must be specified at the interface between the cathode catalyst layer and the membrane to keep the oxygen from entering the membrane. As well, a homogeneous Neumann boundary condition was applied at the interface between the anode catalyst layer and the membrane to prevent hydrogen from entering the membrane.

2.6.3 Solid-Phase Potential Equation

A combination of Dirichlet and Neumann boundary conditions are used to solve the electronic and protonic potential equations. The solid-phase potential equation is

applied in the anode and cathode GDLs and catalyst layers and to account for electron transport in current plates as well. The solid-phase potential ϕ_s is the cell voltage; the value of solid-phase potential along the cathode collector plate edge, i.e., Boundary #5', is prescribed while the value of the cell voltage along the anode current plate edge, i.e., Boundary #5, is assumed to be zero. To represent that no electron current passes through the boundaries, i.e., Boundaries #1,#2,#3,#4,#6,#7,#8,#9 and Boundaries #1',#2',#3',#4',#6',#7',#8',#9'; Homogeneous *Neumann* boundary conditions are applied at these boundaries.

2.6.4 Energy Equations

In this model, a constant temperature, i.e., the ambient temperature T_{am} is applied to the interface between the collector plate and gas diffusion layers at the anode and cathode side. The value of temperature along the boundaries #1, #9 and #1', #9', at anode and cathode side respectively are prescribed; noting that the temperature is higher at cathode than anode side; as well as, it's higher at boundaries #1, #1' than boundaries #9 and #9'. Convective flux conditions are employed at the inlet and outlet of MEA. Otherwise, the thermal insulation conditions are used.

2.6.4 Boundary Conditions for Water and Proton Transport Model

2.6.4.1. Proton transport.

Proton transport through proton-conductive polymer membrane only; thus protons can not go through the GDL and the proton current density at the interface between the catalyst layers and the GDL is set zero. Dirichlet boundary conditions are used to solve the protonic potential equations at the interface between the membrane and

catalyst layers at anode and cathode sides. Elsewhere; homogeneous *Neumann* boundary conditions are applied.

2.6.4.2. Water Transport in the Membrane

In this model; equilibrium is assumed between the gas phase and the membrane phase of water in Nafion membrane. As the water can be transported through the catalyst layers to the membrane; *Dirichlet* boundary conditions should be applied at the interface between the membrane and the catalyst layers at the anode and cathode sides. And the water content at these interfaces can be calculated using [5]:

$$\lambda = 0.043 + 17.8a - 39.85a^2 + 36a^3 \quad \text{for } 0 < a \leq 1 \quad \text{in catalyst layers} \quad (2.88)$$

where a is the activity of water vapor defined as:

$$a = \frac{x_{H_2O}P}{p^{sat}} \quad (2.89)$$

As the water mole fraction exceeds saturation, a linear relation is assumed between the water content and water activity [5]:

$$\lambda = 14 + 1.4(a - 1) \quad \text{for } 1 < a \leq 3 \quad \text{in the membrane} \quad (2.90)$$

the *Neumann* boundary condition is applied at the left and right sides of the membrane:

$$\vec{n} \cdot \vec{\nabla} c_w = 0 \quad (2.91)$$

where \vec{n} denotes the unit vector normal to the boundaries.

2.7 Modeling Parameters

Choosing the right modeling parameters is very important and difficult in establishing the fully PEM fuel cell computational model for numerical simulation. Very limited experimental results are available in the literature with detailed specification of the

cell geometry and experimental conditions. Most of the physical parameters present here and base operation conditions are taken from the modeling work of *Gurau et al.* [7] other available original references are quoted when employed.

Table 2.1 groups the basic dimensions of the computational domain used in this thesis. All values in this table refer to both anode and cathode sides. Table 2.2 lists the base case operational parameters for the current model. Operational parameters have great effects on fuel cell performance and parametric studies will be performed and discussed in details in chapter three.

Table 2.1 Physical dimension of the PEM fuel cell, [7]

PARAMETER	VALUE	UNIT
Gas diffuser width (z-direction)	3×10^{-3}	m
Gas diffuser height (y-direction)	2.54×10^{-4}	m
Collector width	1.3×10^{-3}	m
Catalyst layer thickness	2.87×10^{-5}	m
Membrane thickness (y-direction)	2.3×10^{-4}	m

Table 2.2 Operating parameters for a PEM fuel cell under a base case computation, [7].

DESCRIPTION	VALUE	UNIT
T : fuel cell (ambient) temperature	333	K
ζ_a : stoichiometric ratio at anode	1.3	-
ζ_c : stoichiometric ratio at cathode	3	-
p_a : fuel inlet pressure at anode	1	atm
p_c : air inlet pressure at cathode	3	atm
RH : relative humidity of inlet gas mixture	100	%

The properties for the membrane are required to model various transport phenomena across the membrane. A proper choice of membrane properties will directly improve the accuracy of the modeling work; Table 2.3 lists the electrode properties for the base case. And, Table 2.4 groups the electrochemical parameters chosen for this modeling study.

Table 2.3 Electrode properties

DESCRIPTION	VALUE	UNIT	REF.
ε_g : gas diffuser porosity	0.4	-	[7]
ε_m : membrane porosity	0.28	-	[7]
θ_{mc} : volume fraction membrane in catalyst	0.5	-	[7]
k_p : permeability to air in the gas diffuser	1.76×10^{-11}	m^2	[7]
k_h : hydraulic permeability of the membrane	1.58×10^{-18}	m^2	[7]
k_ϕ : electrokinetic permeability of membrane	1.13×10^{-19}	m^2	[7]
k_{air} : air thermal conductivity	3.0×10^{-2}	$W / m / K$	[7]
k_{gr} : thermal conduc. of matrix of gas diffuser	150.6	$W / m / K$	[7]
$k_{m,dry}$: thermal conductivity of dry membrane	100	$W / m / K$	[7]
$c_{p,air}$: air specific heat at constant pressure	1008	$J / kg / K$	[7]
c_f : fixed charged site concentration in memb.	1.2×10^3	mol / m^3	[7]
z_f : charge of sulfonate site in memb.	-1	-	[7]
ρ_m^{dry} : membrane solid dry mass density	1980	kg / m^3	[7]
EW_m : equivalent membrane weight	1.1	kg / mol	[5]
f : membrane swelling coefficient	0.0126	-	[5]

Table 2.5 listed the values of binary diffusivities involved in Maxwell-Stephan equations (2.11). These values are determined experimentally under the specific reference temperature and 1 atm pressure and now should be converted to actual operating conditions used in this study by conversion Eq. (2.10).

To visualize the mesh element quality in the 2D case, mesh quality for all elements over the entire computational domain is shown in Figure 2.6. The quality measure is related to the aspect ratio, which means that anisotropic elements can get a low quality measure even though the element shape is reasonable. For triangular elements, COMSOL Multiphysics computes the mesh quality q with the formula:

$$q = \frac{4\sqrt{3}A}{h_1^2 + h_2^2 + h_3^2} \quad (2.92)$$

where A is the area, and h_1 , h_2 and h_3 are the side lengths of the triangle. The value of q is a number between 0 and 1. If $q > 0.3$, the mesh quality should not affect the solution's quality [47]. Figure 2.6 shows the minimum quality of the mesh element is 0.447, which is greater than 0.3.

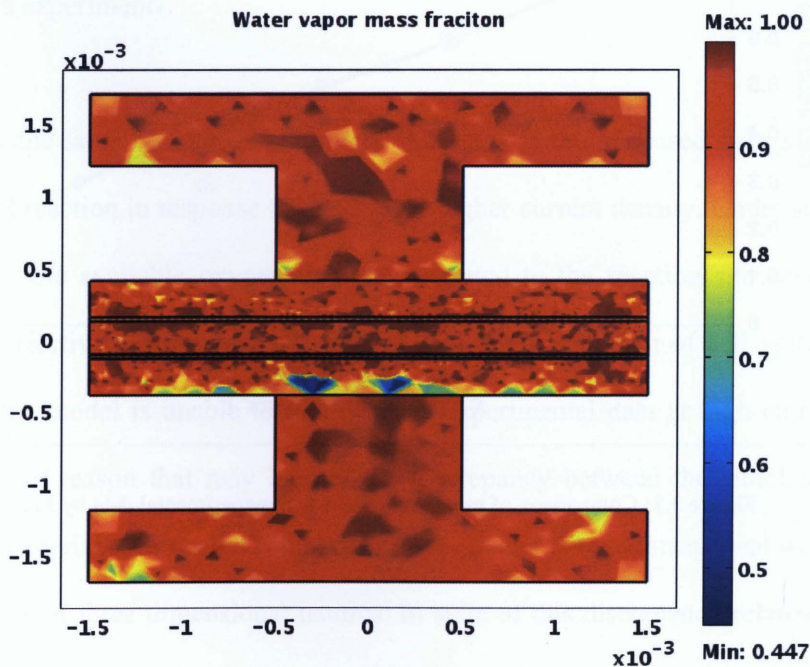


Figure 2.6: Mesh quality of computational domain.

Chapter 3

Base Case Results and Parametric Study

3.1 Model Validation

To validate the fuel cell model presented in this thesis, a comparison using fuel cell performance curves is made between the simulation results corresponding to the base case conditions (Table 2.2) and the experimental data obtained by [46].

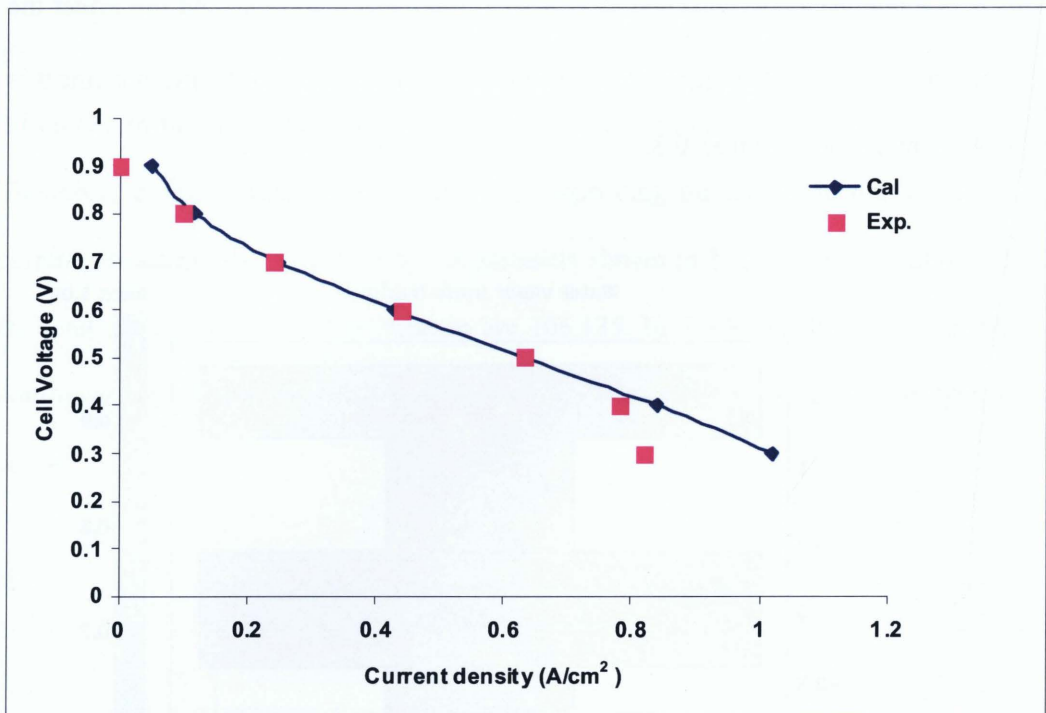


Figure 3.1: Comparison of modeling results with experimental data by Ju and Wang

].

The polarization curve is the most important characteristic of a fuel cell. It may be used for diagnostic purposes. As shown in Figure. 3.1, the slope of the polarization curve is steeper and exhibits slight nonlinearity in the range of $0.065 A/cm^2 \leq |\bar{i}| \leq 0.246 A/cm^2$, which represents the activation region. Then, the

two sets of results have good agreement at intermediate current densities $0.246 \text{ A/cm}^2 \leq |\bar{i}| \leq 0.632 \text{ A/cm}^2$, showing the cell voltage drops clearly in a linear trend as the current density increases within this ohmic loss region.

However, a remarkable discrepancy is found for high current densities ($|\bar{i}| \geq 0.632 \text{ A/cm}^2$). This is due to lack of an established mathematical model to accurately quantify the effect of mass transport losses. As of today, all existing fuel cell models underestimate the mass-transport limitation. The limiting current density effect can be practically observed in the numerical results by examining the starting point of a new steeper drop of cell voltage following the generally linear ohmic loss region. As shown in Figure 3.1, the limiting current density captured from the simulation results is about 0.8 A/cm^2 , which is in fairly good agreement with the finding through experiments.

The reason for the latter steeper drop in the cell voltage is the increased strength of electrochemical reaction in response to the desired higher current density. Under such a circumstance, the available oxygen that has migrated to the reaction site cannot afford a fully effective electrochemical reaction, causing a limitation of cell voltage output. Thus, the model is unable to replicate the experimental data at high current densities. Another reason that may lead to the discrepancy between the simulation results and the experimental results is that the present model is two dimensional while the experiment is of three dimensional natures. In spite of this discrepancy related to the limiting current density, the model can efficiently predict the overall performance of an operational fuel cell under its normal working conditions.

Apart from polarization curve, the evolution the power density along with varying current density is another commonly used curve in fuel cell technology. The results obtained from computer model and experiments are plotted in Figure 3.1 Good agreement between the two sets of results persists up to a current density of $0.632 A/cm^2$. For high current densities ($|i| \geq 0.632 A/cm^2$), increasing discrepancy is observed. This is again due to the concentration losses caused by the reactant transport limitation in the region near and beyond the limiting current density.

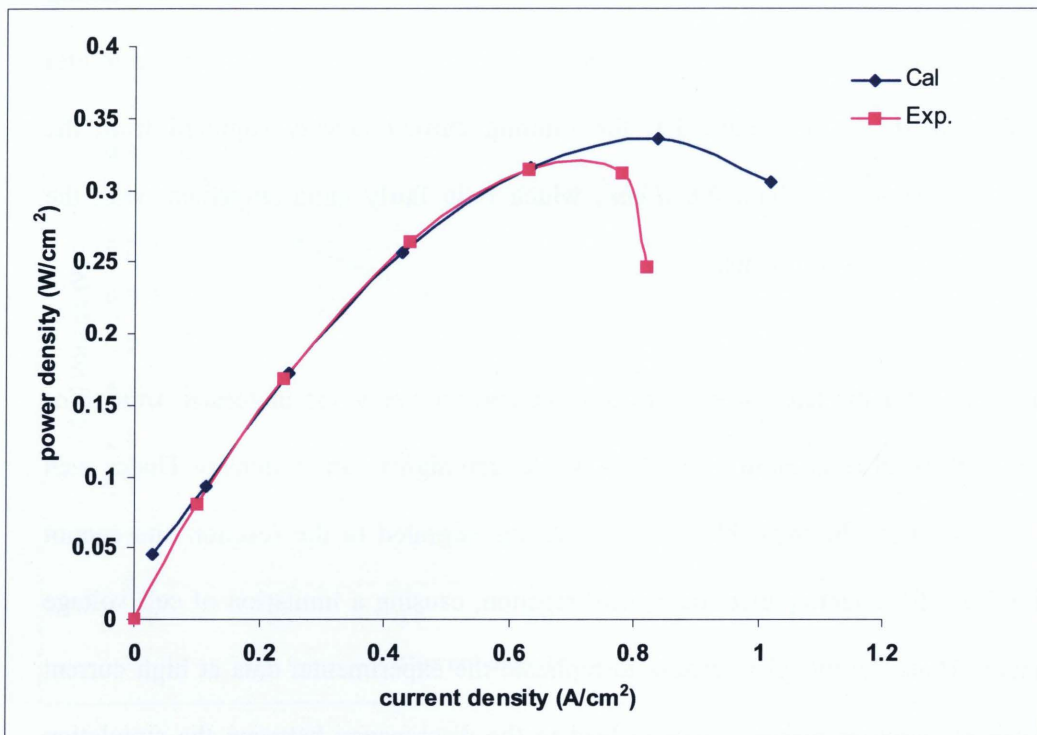


Figure 3.2: Power curve resulting from the fuel cell polarization curve.

The power curve resulting from the fuel cell model helps identify the limiting current density. Also, Figure 3.2 shows that there is a maximum power density ($0.316 W/cm^2$) when employing a fuel cell. Hence, it does not make sense to pursue the operation of

fuel cell beyond its maximum power point; instead, optimal fuel cell performance takes place at a combination of a lower current and a higher cell voltage.

3.2 Base Case Study on Thermodiffusion Effect.

A temperature gradient applied to a liquid mixture not only causes a heat flux but also gives rise to a diffusion current of the constituent components. This research is focused on the study of the thermodiffusion effect in the mixture of hydrogen, water vapor and carbon dioxide at the anode side and oxygen, water vapor and nitrogen at the cathode side of the polymer electrodes membrane PEM fuel cell, aiming at an understanding of the dependence of molar fractions on thermodiffusion. Two models will be studied and compared: the first one takes thermodiffusion into account and the other model neglects it. The numerical simulation employs fuel cell operational conditions as described in Table 2.2. Numerical results such as the distribution of mole fractions of reactant gases will be examined in the subsequent sections.

3.2.1 Oxygen Distribution

Figure 3.3 shows the mole fraction of oxygen at 0.7 V cell voltage in the y-z plane for PEM fuel cells with thermodiffusion (Figure 3.3a) and without thermodiffusion (Figure 3.3b). The only mechanism for mass transport is diffusion; hence, the oxygen decreases in the direction toward the reaction surface and the minimum value can be found in the centre of the domain, indicating a greater concentration gradient in the z-direction within the GDL and CL as a result of the presence of the current plate separating the gas channels. Since the geometry is symmetric, the resulting distribution also appears symmetric about its vertical central line.

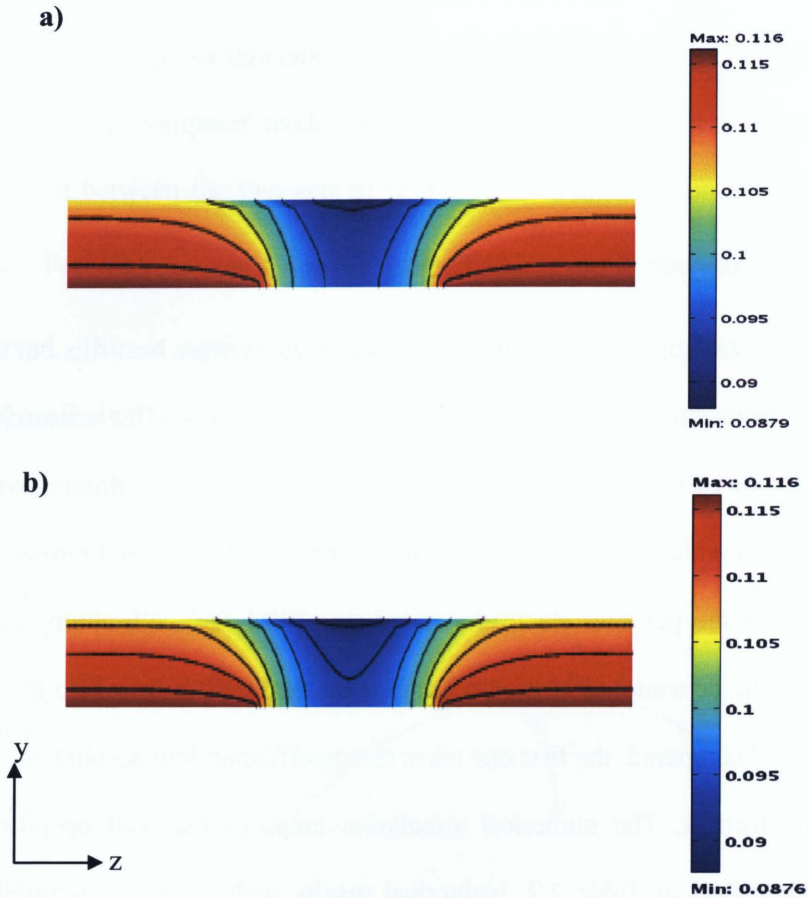


Figure 3.3: Oxygen mole fraction in y-z plane for cell voltage 0.7V: (a) with thermodiffusion DT and (b) without thermodiffusion

To further analyze the cell performance, the oxygen mole fraction is plotted at the gas diffusion layer as a function of cell height (y) as in Figure 3.4. The plotted oxygen mole fraction profile corresponds to $y = -2.6 \times 10^{-4}$ m. It is noticed that the consumption of the oxygen mole fraction becomes 3.4% more when the thermodiffusion is taken into account, indicating an underestimation of oxygen consumption if the thermodiffusion is ignored.

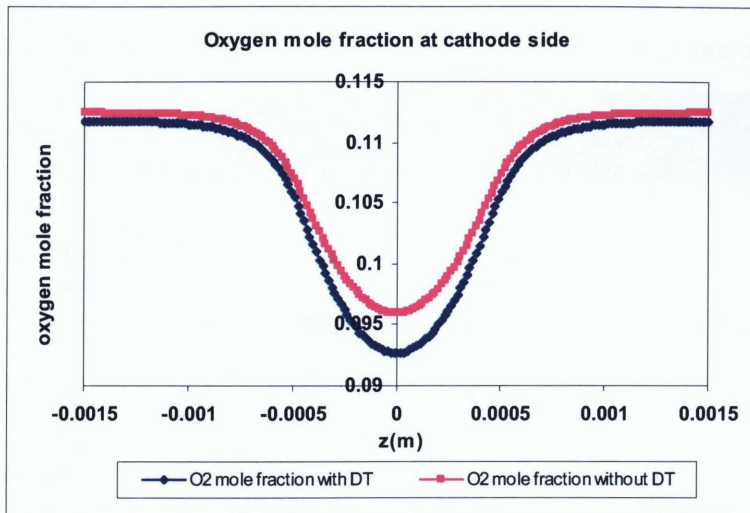


Figure 3.4: Comparison of oxygen mole fraction with and without thermodiffusion DT at cathode side.

3.2.2 Water Vapour Distribution at Cathode Side

Figure 3.5 demonstrates the water vapour mole fraction distribution at the cathode side. The contours for both cases illustrate that the water increases linearly in the direction toward the reaction surface, and the profile is symmetric about its vertical central line due to the symmetric geometry and flow employed. In addition, it is noticed that the maximum value of the water vapour mole fraction within the GDL and cathode catalyst layers decreases from 0.276 to 0.275 when the thermodiffusion is switched on.

Figure 3.6 indicates that the water vapour mole fraction increases by 1.931% at $y = -2.6e-4m$, which is the same position as in Figure. 3.4. Consistent with each other, the more oxygen depleted, the higher water vapour concentration produced.

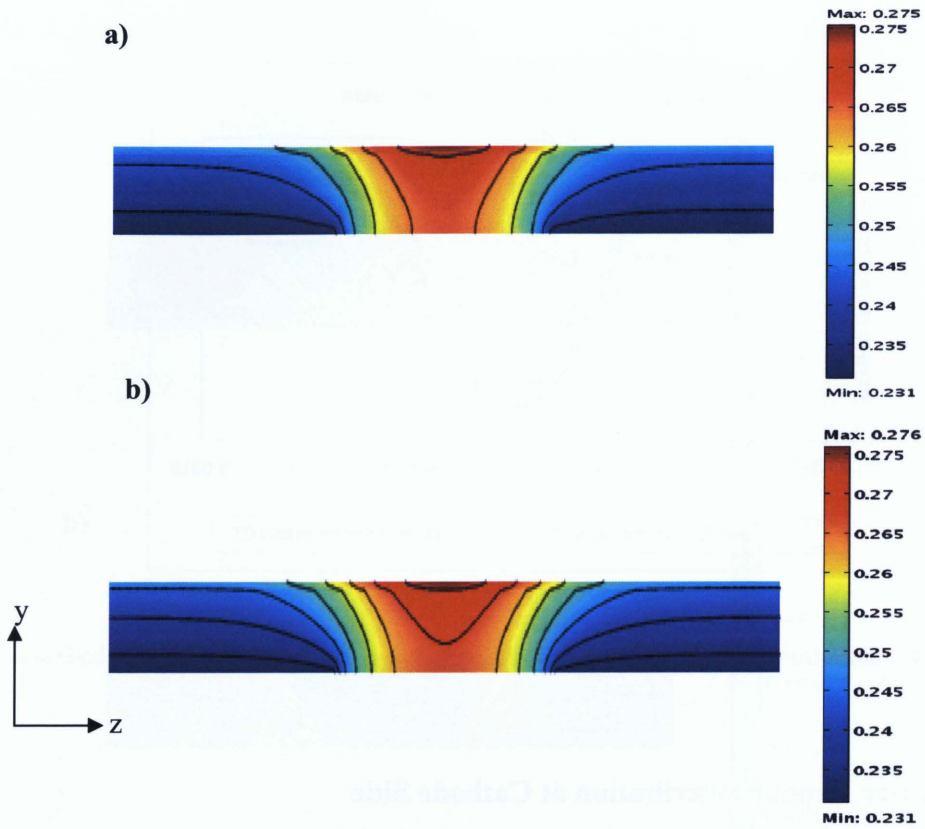


Figure 3.5: Water vapour mole fraction for cell voltage 0.7V: (a) with thermodiffusion DT and (b) without thermodiffusion

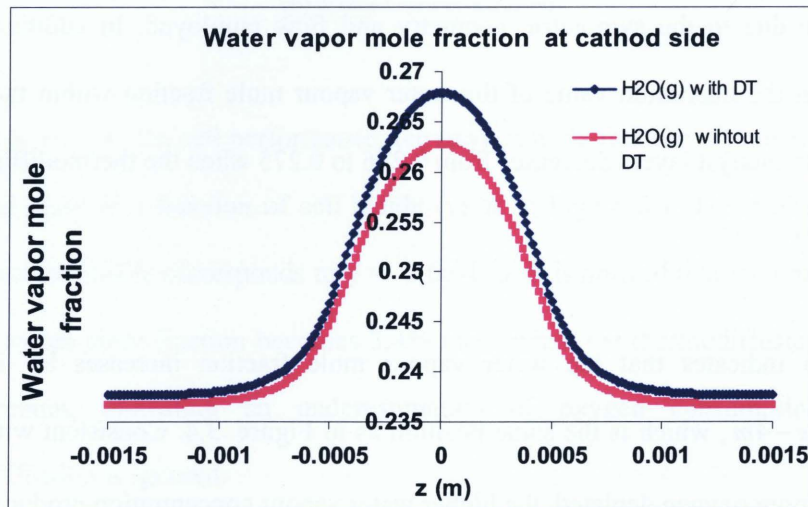


Figure 3.6: Comparison of water vapor mole fraction with and without thermodiffusion DT at cathode side.

3.2.3 Hydrogen and Water Vapour Distribution at the Anode Side

Figure 3.7 depicts the water vapour mole fraction distribution at the anode side; it shows the maximum of the water vapour mole fraction slightly decreases when taking the thermodiffusion into account. Furthermore, Figure 3.8 shows that the difference is as little as 0.026% only. Therefore, there is no significant effect on the hydrogen mole fraction, revealing the anode turned out to be less sensitive to the addition of thermodiffusion.

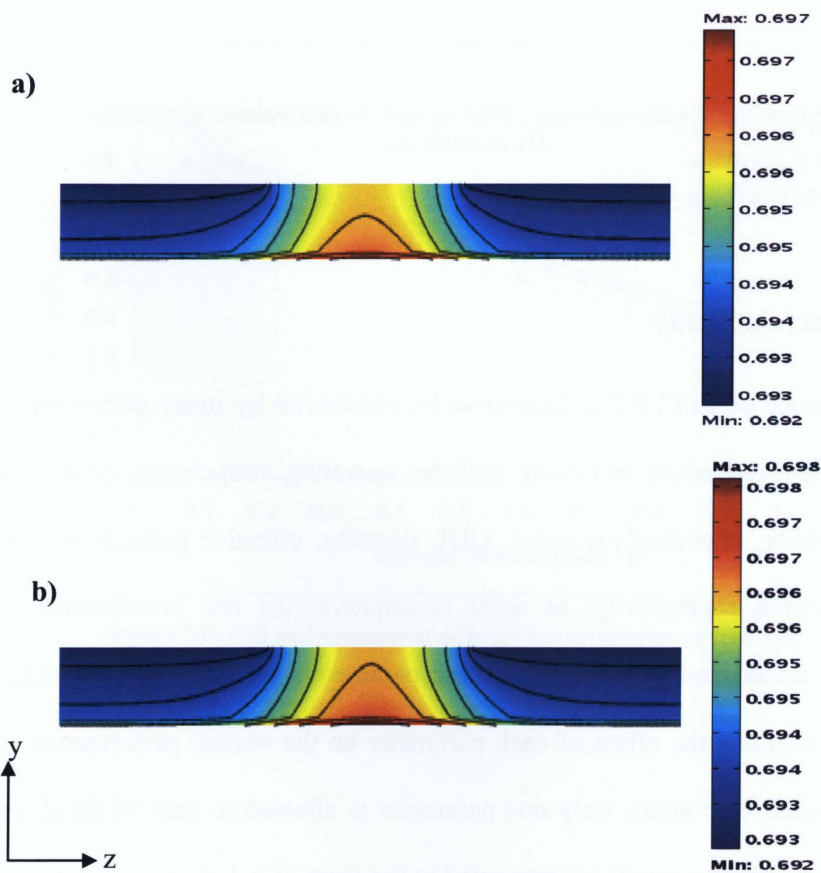


Figure 3.7: Water vapor mole fraction at anode side for cell voltage 0.7V: (a) with thermodiffusion DT and (b) without thermodiffusion (b)

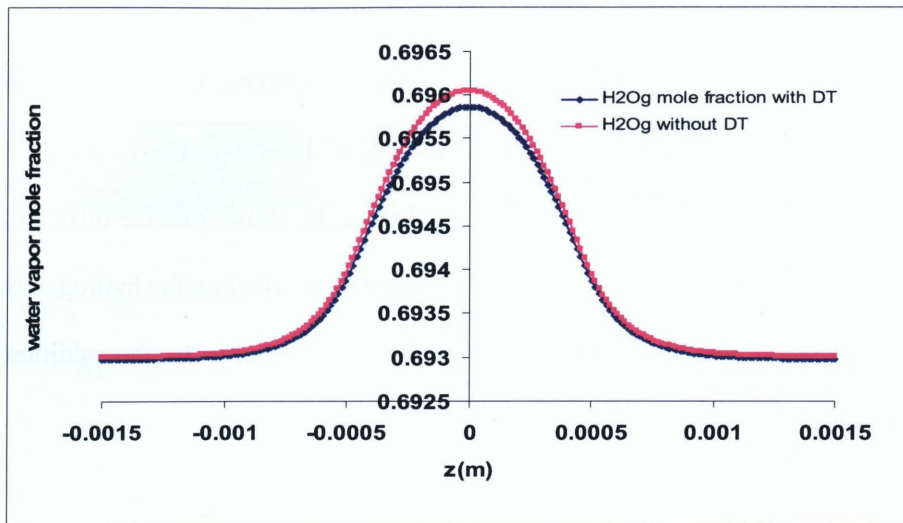


Figure 3.8: Comparison of water vapor mole fraction at anode side with and without thermodiffusion DT at anode side

3.3. Parametric Study

The performance of PEM FC is known to be influenced by many parameters. The parameters investigated in this study include: operating temperature, inlet reactant relative humidity, operating pressures, GDL porosity, effective porosity of catalyst layer, and proton conductivity. In order to improve fuel cell performances, it is necessary to understand the effects of these parameters on fuel cell operations. To individually examine the effect of each parameter on the overall performance of the fuel cell, in each case study, only one parameter is allowed to vary while all others remain unchanged. The results are presented in the form of polarization curve.

3.3.1. Effect of Operating Pressure Load.

A fuel cell can be operated at ambient pressure or in a pressurized state. Fuel cell performance will improve with increased pressure. Figure 3.9 shows polarization curves for three different pairs of testing pressure conditions: P (1-1), that is, 1atm at

the anode side and the cathode side as well; P (1-3), which is 1atm at the anode side and 3atm at the cathode side, and P (3-5) representing 3atm at the anode side and 5atm at the cathode side. Figure 3.9 illustrates that, as the operating pressure rises, the fuel cell performance improves, that is, properly pressurized reactant gas streams will help increase the limit current density.

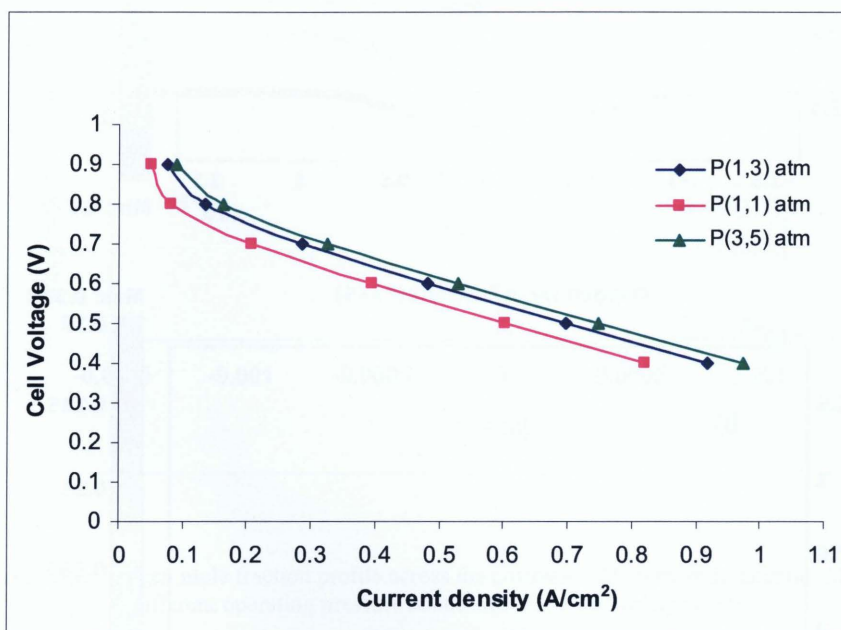


Figure 3.9: Cell performances at different operating pressure loadings.

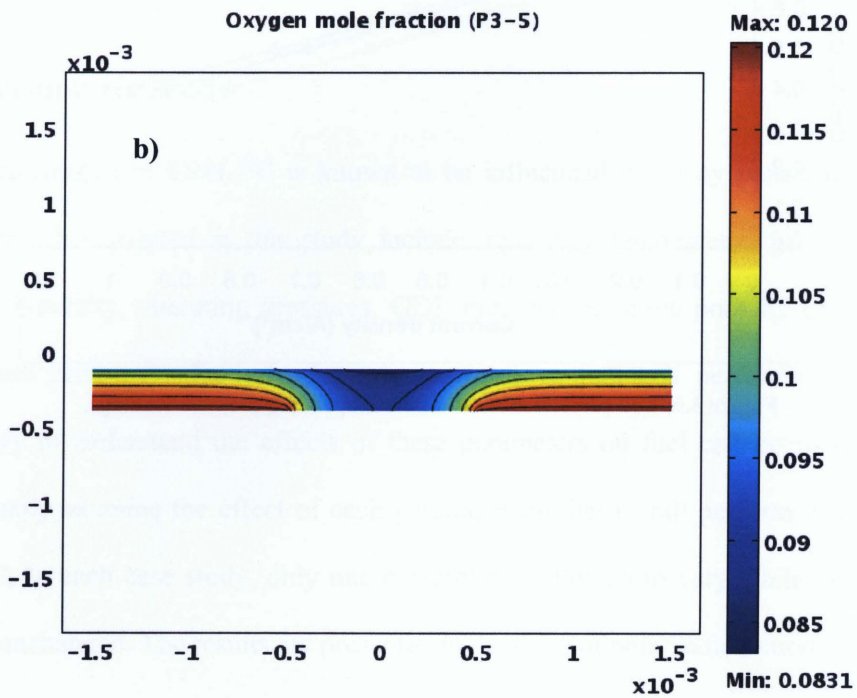
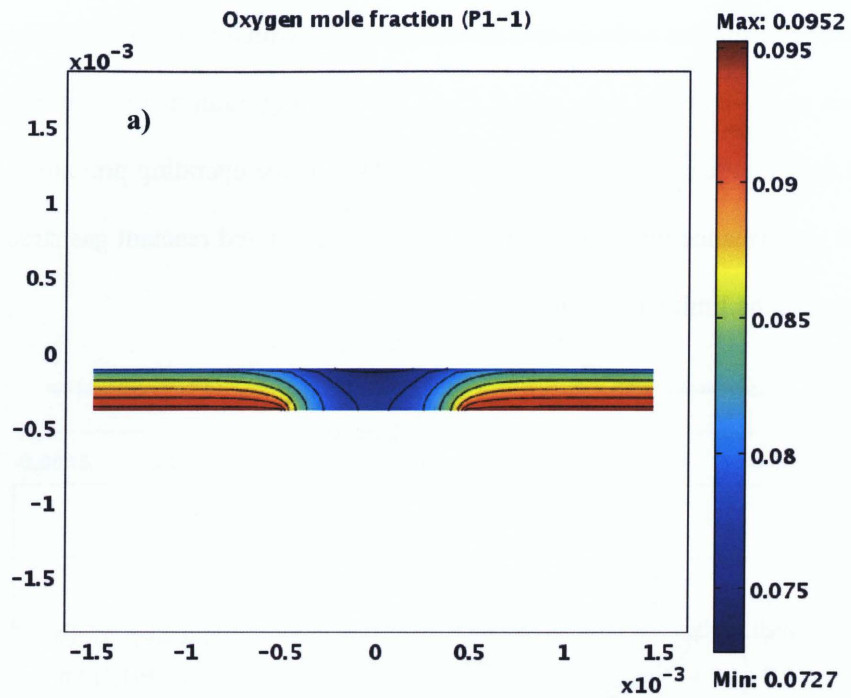


Figure 3.10: Oxygen mole fraction distribution under different operating pressure conditions at the cell voltage 0.6V.

Figures 3.10 and 3.11 clearly demonstrate that more oxygen is supplied when pressurization applies to both sides of the fuel cell. Figure 3.11 shows the oxygen mole fraction distribution across the gas diffusion layer at the cathode side corresponding to $y = -2.6e-4$.

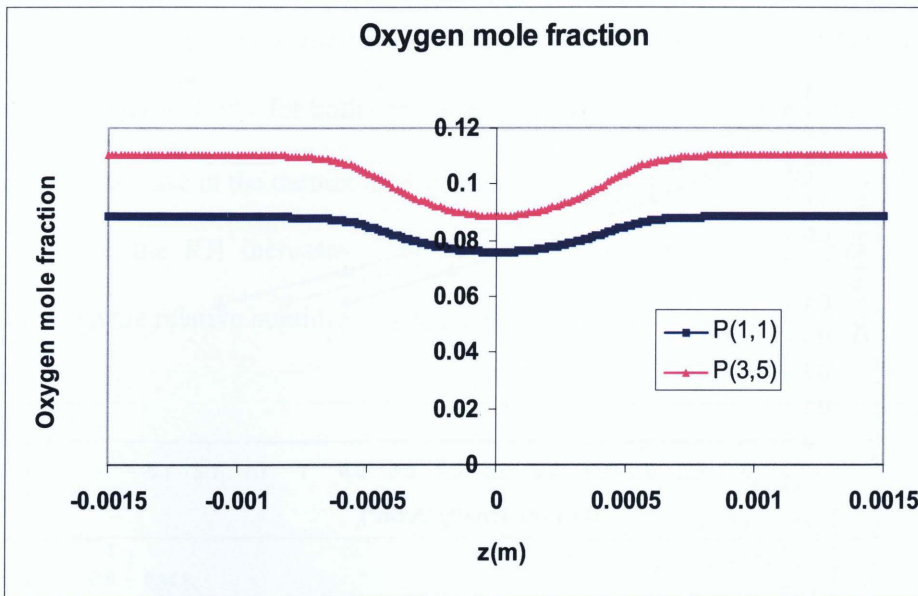


Figure 3.11: Oxygen mole fraction profile across the channel-GDL domain at cathode side under different operating pressure conditions at the cell voltage 0.6V.

3.3.2. Effect of temperature

The cell temperature is another operating parameter that may be selected and preset. In general, a reasonably raised operating temperature results in higher cell potential. Based on the experimental studies, Wang *et al* [48] concluded that when sufficient humidification is ensured, the performance of the PEM fuel cell improves with the increase of operating temperature. Their finding is confirmed by this numerical investigation, as shown in Figure 3.12. A higher temperature causes more

vaporization of water product, leading more waste heat to the form of latent heat and less liquid water for removal from the fuel cell. The upper limit of operation for PEMFCs is about 90°C (363K) because water evaporates from the membrane and performance drops quickly if overheated.

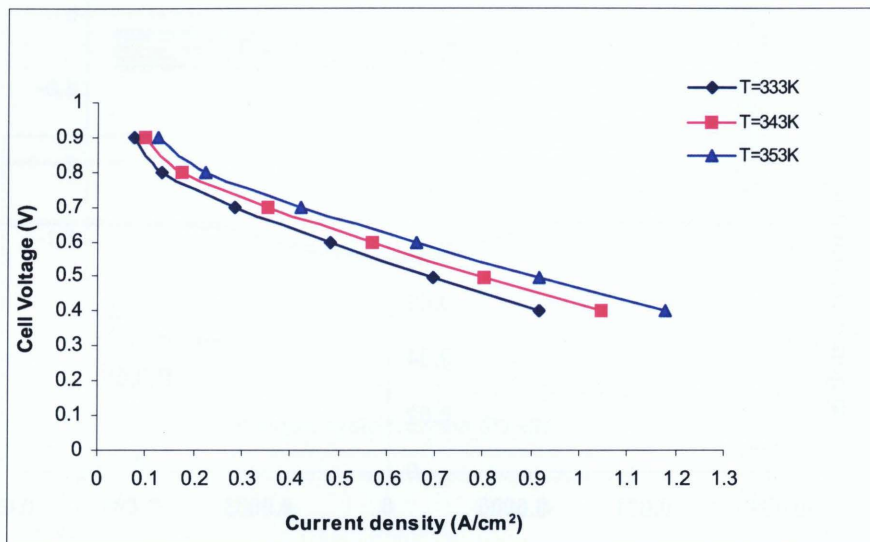


Figure 3.12: Effect of temperature on fuel cell performance.

Figure 3.12 illustrates the polarization curves of a PEMFC at three operating temperatures between 333 K and 353 K. The limit current density increases with the increase of the fuel cell temperature. Gas diffusivity and membrane conductivity go up in the case of a higher temperature, resulting in better mass transport. On the contrary, at lower temperatures, water is in its liquid state, and may flood the catalyst and gas diffusion layers, which may adversely affect gas diffusivity. However, membrane conductivity may decrease at high temperatures due to the reduction of water content in the membrane.

3.2.3 Effect of Relative Humidity

Relative humidity is the ratio of the partial pressure due to water vapour to the saturation pressure, which is the maximum amount of water vapour that can be present in gas for given conditions [48], [49]. In PEM fuel cell, the reactant gases need to be humidified before entering the cell for high ionic conductivity of the membrane. The polarization curves for different inlet reactant relative humidity, ranging from 50% to 100% for both oxygen and hydrogen, are shown in Figure 3.13. A significant increase in the current density from 0.2597 A/cm^2 to 0.9179 A/cm^2 is achieved when the RH increases from 50% to 100%. The best performance is obtained when the relative humidity reaches 100%.

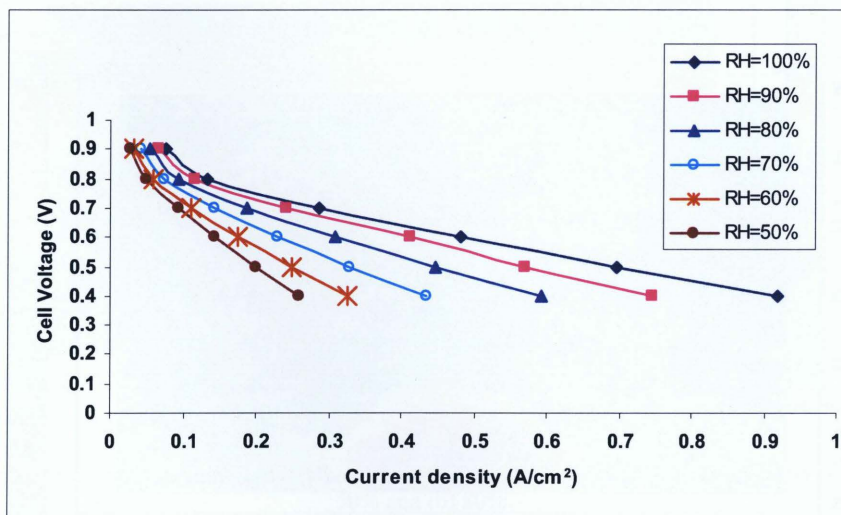


Figure 3.13: Polarization curves corresponding to different relative humidity

At high relative humidity (RH), the ionic conductivity of a Nafion117 proton exchange membrane increases with membrane water content as suggested by Eq. (2.80), which helps reduce the membrane-phase potential loss as demonstrated in Figures 3.14 and 3.15.

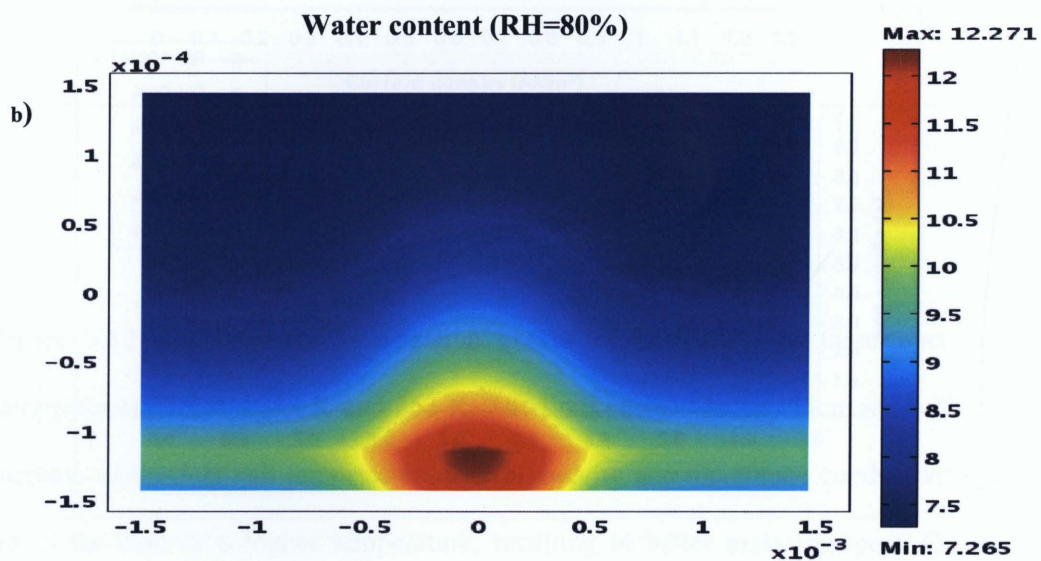
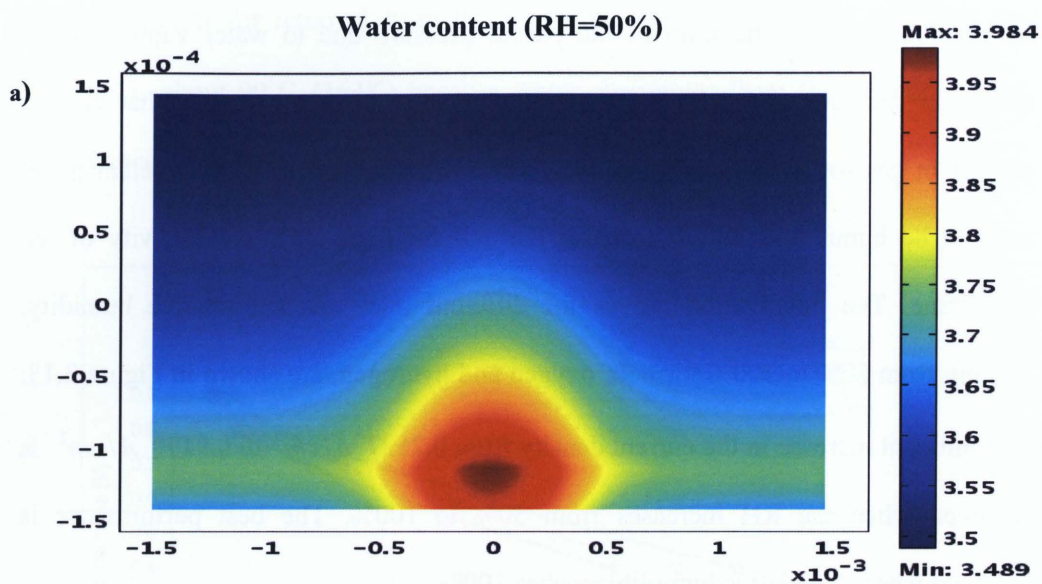
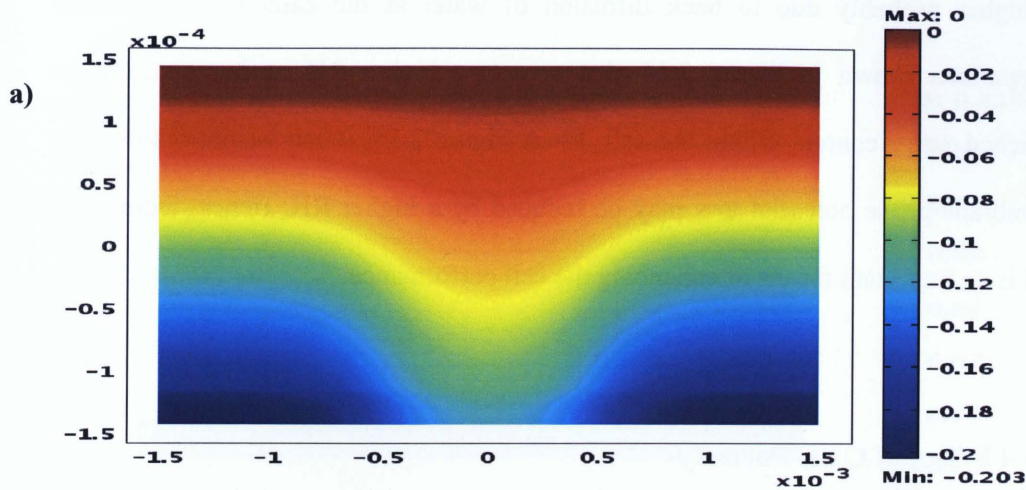


Figure 3.14: water content at cell voltage 0.6V, and Relative humidity RH: (a) 50% and (b) 80%.

Membrane-phase potential (V) (RH=50%)



Membrane-phase potential (V) (RH=80%)

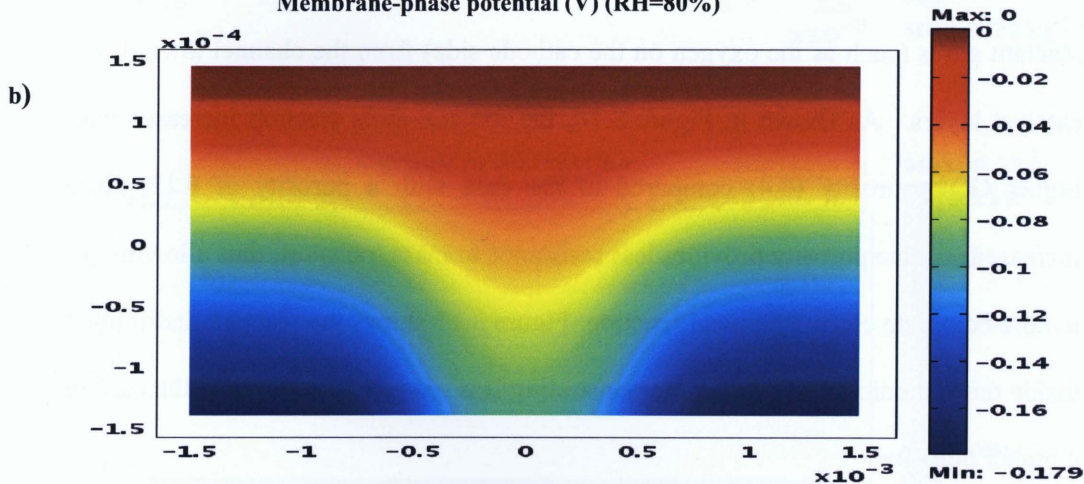


Figure 3.15: membrane-phase potential losses at cell voltage 0.6V, and relative humidity (RH): (a) 50% and (b) 80%.

The water is produced at the catalyst layer on the cathode side as result of the electrochemical reaction expressed in Eq. (1.4). [50], [51], indicated that liquid water pockets are more likely to form under the land area of the gas diffusion layer, and their finding is confirmed by this study, as shown in Figure 3.14. More accumulation of water content is found near to the current collector where the mass fraction of water

is higher probably due to back diffusion of water at the cathode side. Overall comparison shown in Figure 3.14 also reveals a higher RH renders much more enriched water content within the cell. From Figure 3.15, it can be noticed that the membrane-phase potential loss may be reduced by a higher RH. Hence, increase of RH is an important means of enhancing the cell performance.

3.3.4 Effect of GDL Porosity

The porosity of a material is the ratio of void space to the total volume of the material. Fuel cell electrodes and catalyst layers must exhibit good porosity in order to be effective. Higher volume porosity has positive effects on the mass transport of reactant gases (such as the oxygen on the cathode side) from the channel towards the catalyst layers. As shown in Figure 3.16, the oxygen mole fraction increases with higher GDL porosity (0.4) compared to the case with a porosity of 0.17, since increased volume porosity provides less resistance to mass transport, thus allowing for a more complete electrochemical reaction. Figure 3.17 shows the reactant distribution inside the cathodic catalyst layer, demonstrating less oxygen is left over in the case of a higher porosity.

The simulation results of the effects of GDL porosity on fuel cell performance are shown via polarization curves in Figure 3.18 for two different GDL porosities of 0.17 and 0.4. Consistent with the previous two figures, Figure 3.18 reveals again that a higher GDL porosity results in a higher limit current density.

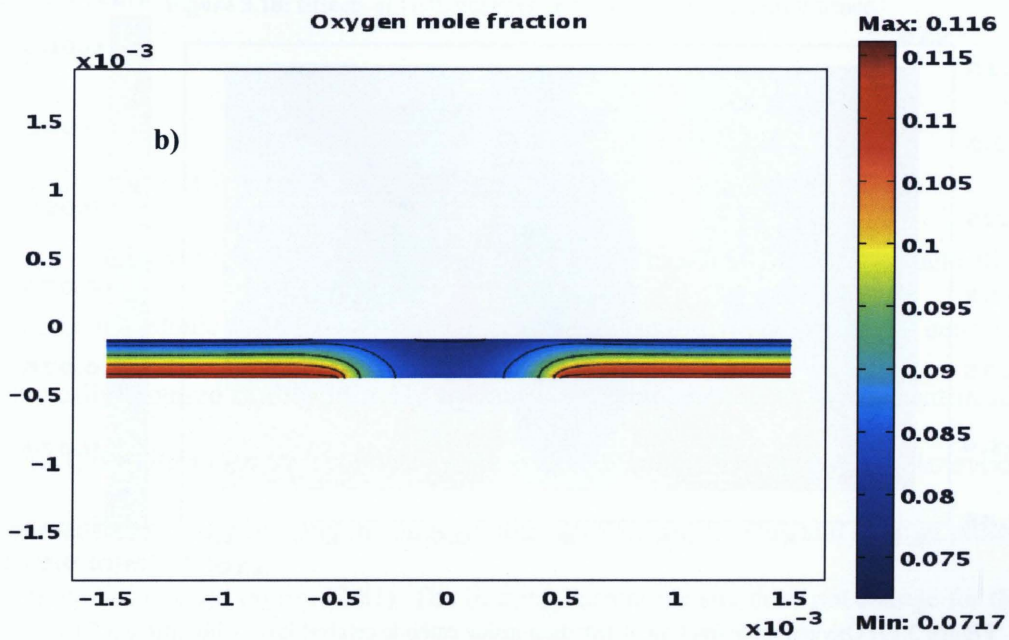
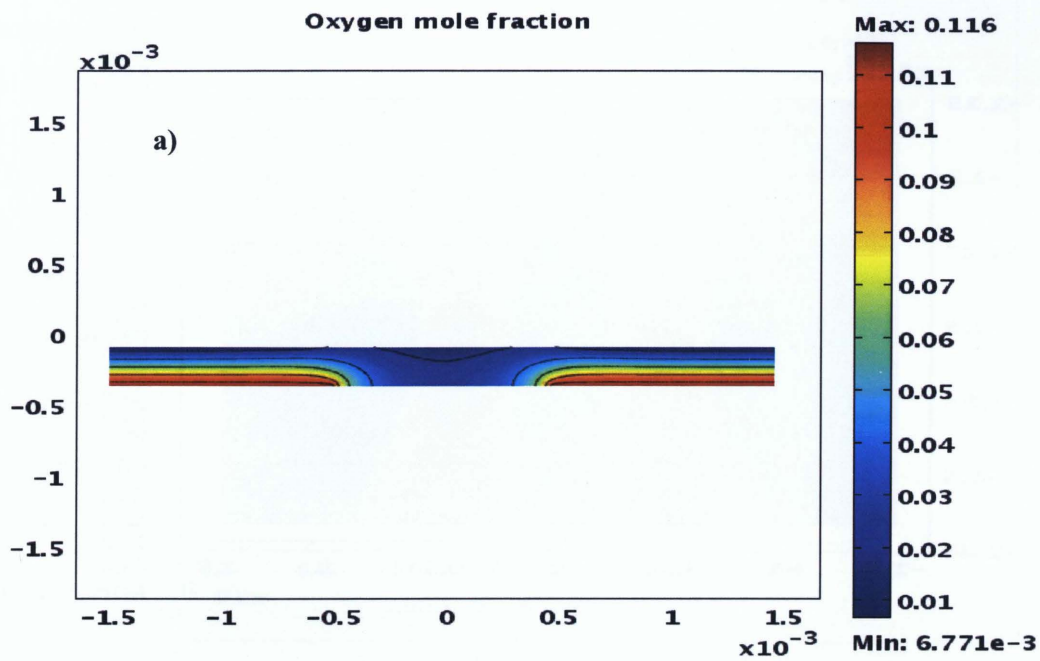
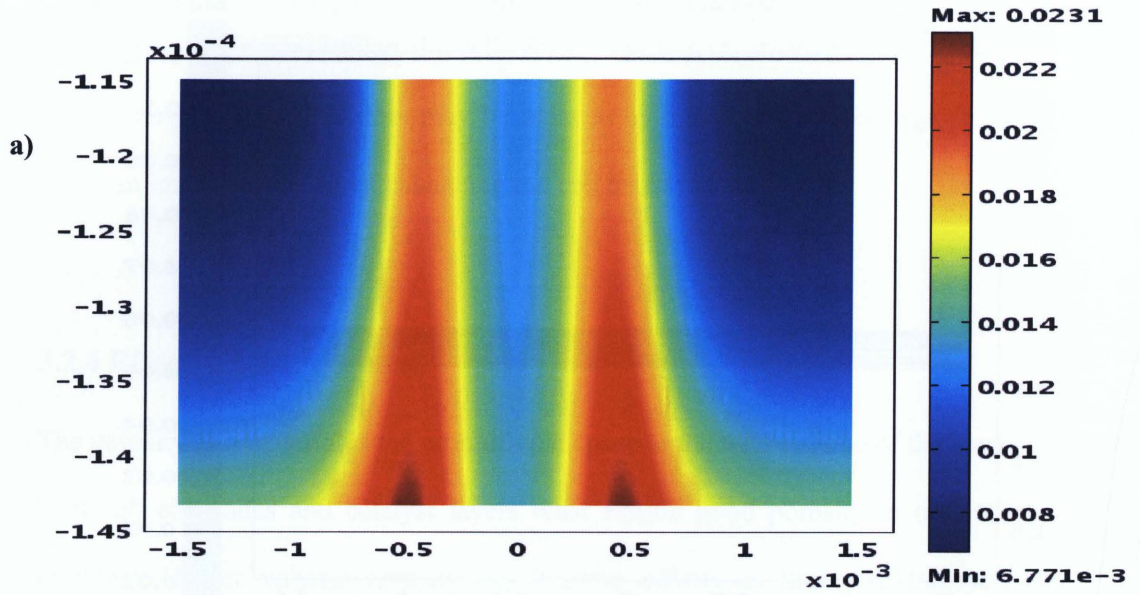


Figure 3.16: Oxygen mole fraction distribution inside fuel cells with different GDL porosities: (a) $\varepsilon_g = 0.17$, and (b) $\varepsilon_g = 0.4$ at cell voltage 0.4V.

Oxygen mole fraction in the cathode catalyst layer



Oxygen mole fraction in the cathode catalyst layer

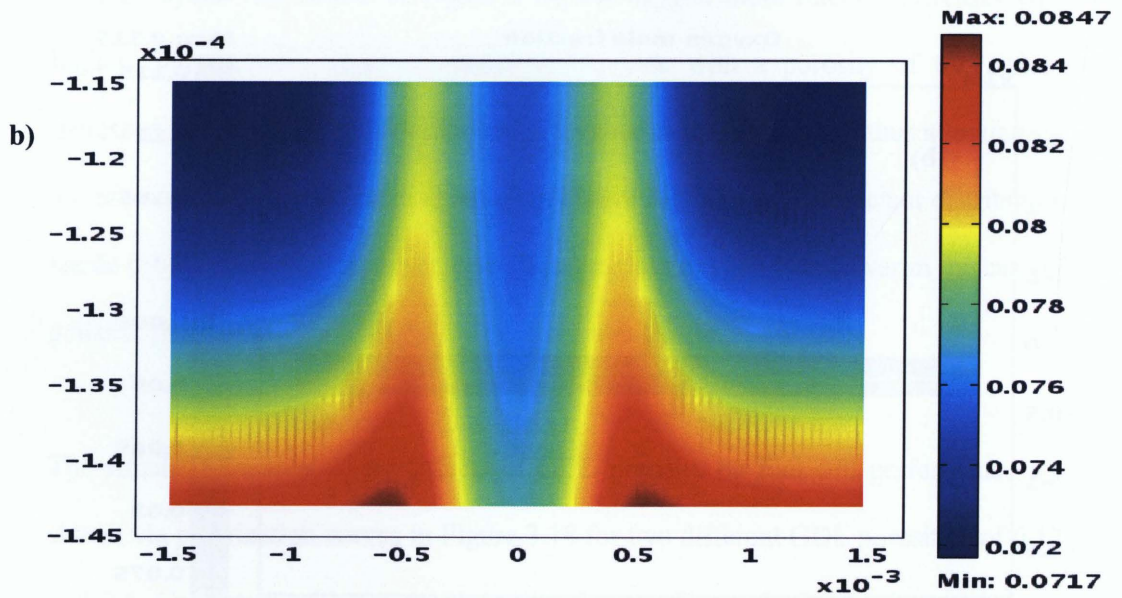


Figure 3.17: Oxygen mole fraction distribution inside cathode catalyst layer with different GDL porosities: $\varepsilon_g = 0.17$ (a) and $\varepsilon_g = 0.4$ (b) at cell voltage 0.4V.

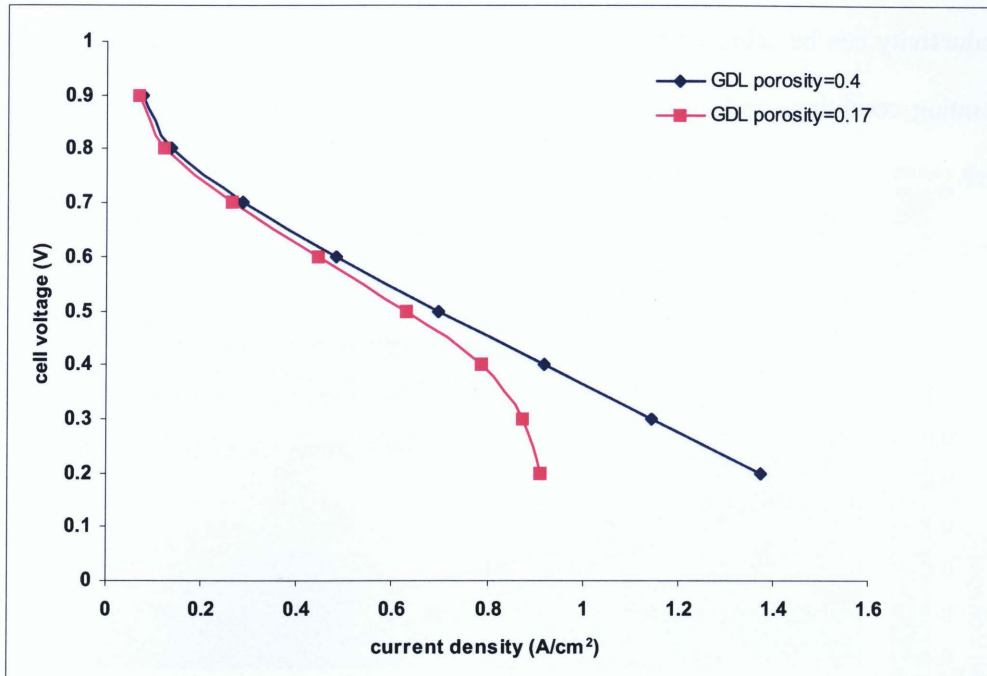


Figure 3.18: Effects of GDL porosity on the PEM fuel cell performance.

3.3.5 Effect of Proton Conductivity

One of the most important properties of the polymer membranes used in a fuel cell is the high protonic conductivity under the hydrated condition and at current densities typically required in PEMFCs. By assuming the proton conductivity constant inside MEA, the effect of proton conductivity is studied. Figure 3.19 depicts the polarization curves for two constant proton conductivities, 10 S/m and 14 S/m, and altering proton conductivity based on Eq. (2.81). The limiting current density does not change for the constant proton conductivity of 10 S/m and the varying proton conductivity based on Eq. (2.81). However, fuel cell can better perform if a higher proton conductivity of 14 S/m is employed. The comparison shown in Figure 3.19 indicates that the overall

current density is decreasing when the proton conductivity goes lower. High proton conductivity can be achieved by increasing water content, which is mainly related to operating conditions and another design parameter, ionomer fraction in the catalyst layer.

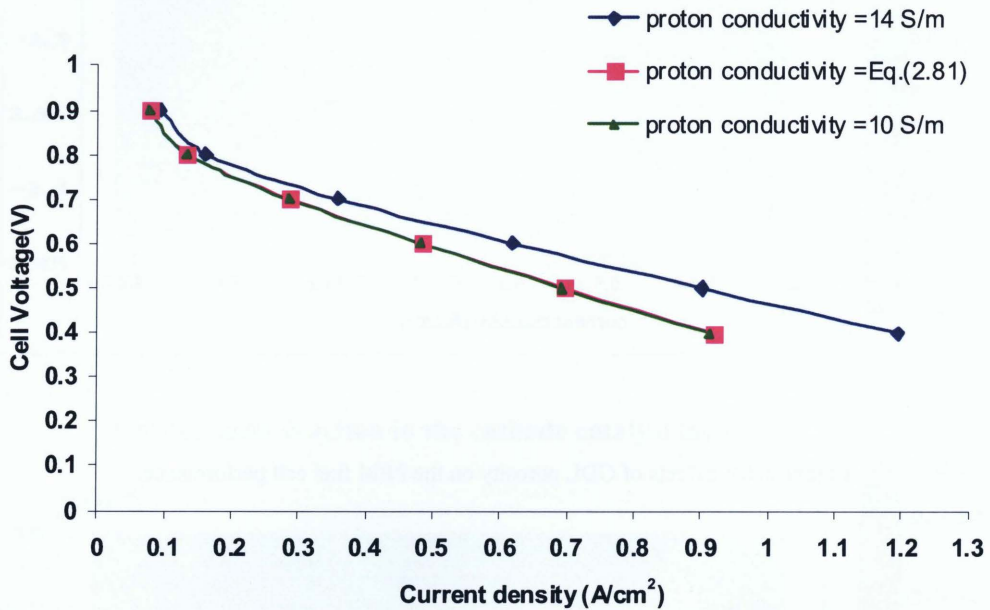


Figure 3.19: Effect of proton conductivity on PEM fuel cell performance.

To achieve a desired current density, various potential losses should be reduced. Due to ohmic resistance, there is a potential loss in the electrolyte phase from the catalyst layer/membrane interface to the catalyst layer/diffuser interface. Also, the potential loss in the membrane is due to resistance to proton transport across the membrane. The membrane phase potential loss increases from 0.155 V to 0.165 V with the decrease of proton conductivity from 14 S/m to 10 S/m, as shown in Figure 3.20. This

signifies that higher proton conductivity can reduce the proton resistance in the membrane.

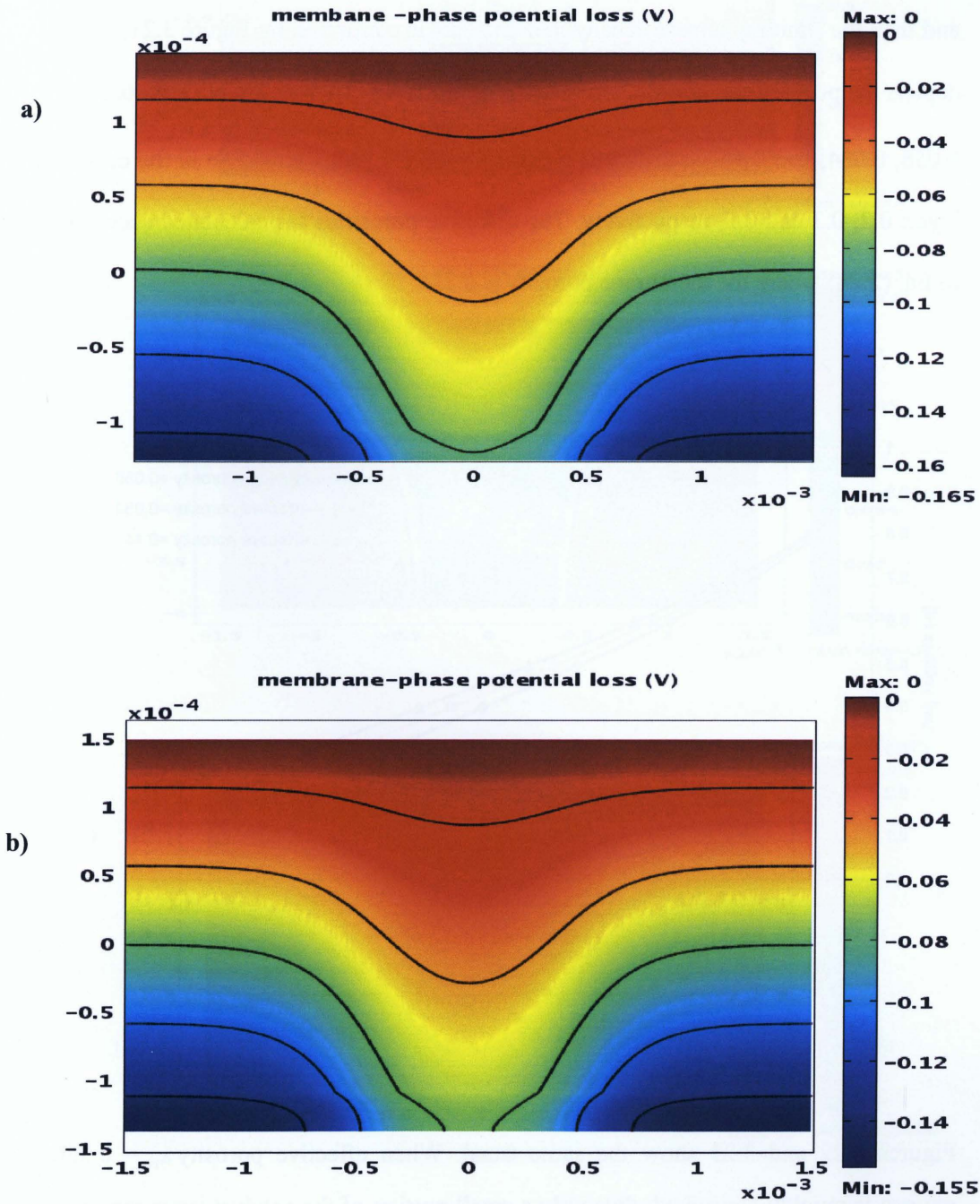


Figure 3.20: Membrane-phase potential losses for different proton conductivities: (a) 10 S/m and (b) 14 S/m, at cell voltage 0.6V

3.3.6 The effects of effective porosity of the catalyst layer

The oxygen transport resistance depends on the effective porosity of the catalyst layer. If the effective porosity of the catalyst layer is high, oxygen transfer resistance is low and then the limiting current density is high. This is confirmed by Figure 3.21, which depicts the polarization curves, corresponding to a three different effective porosity ε_{ct} : 0.056, 0.084, and 0.14 for different volume fractions of the membrane in the catalyst layer: 0.2, 0.3 and 0.5, respectively. The effective porosities are calculated according to Eq. (2.28) where the membrane porosity is 0.28.

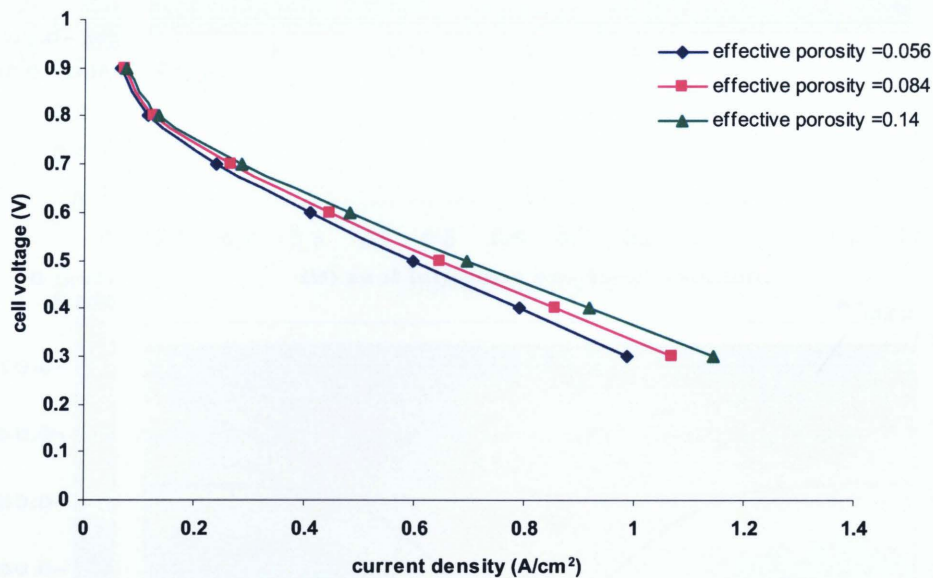


Figure 3.21: The influence of effective porosity on the performance of the PEM fuel cell.

Figures 3.22 and 3.23 show the same trend. When effective porosity $\varepsilon_{ct} = 0.056$, oxygen is quickly consumed, thus only a small portion of the catalyst layer can serve actively. When $\varepsilon_{ct} = 0.14$, more area of catalyst layer become active.

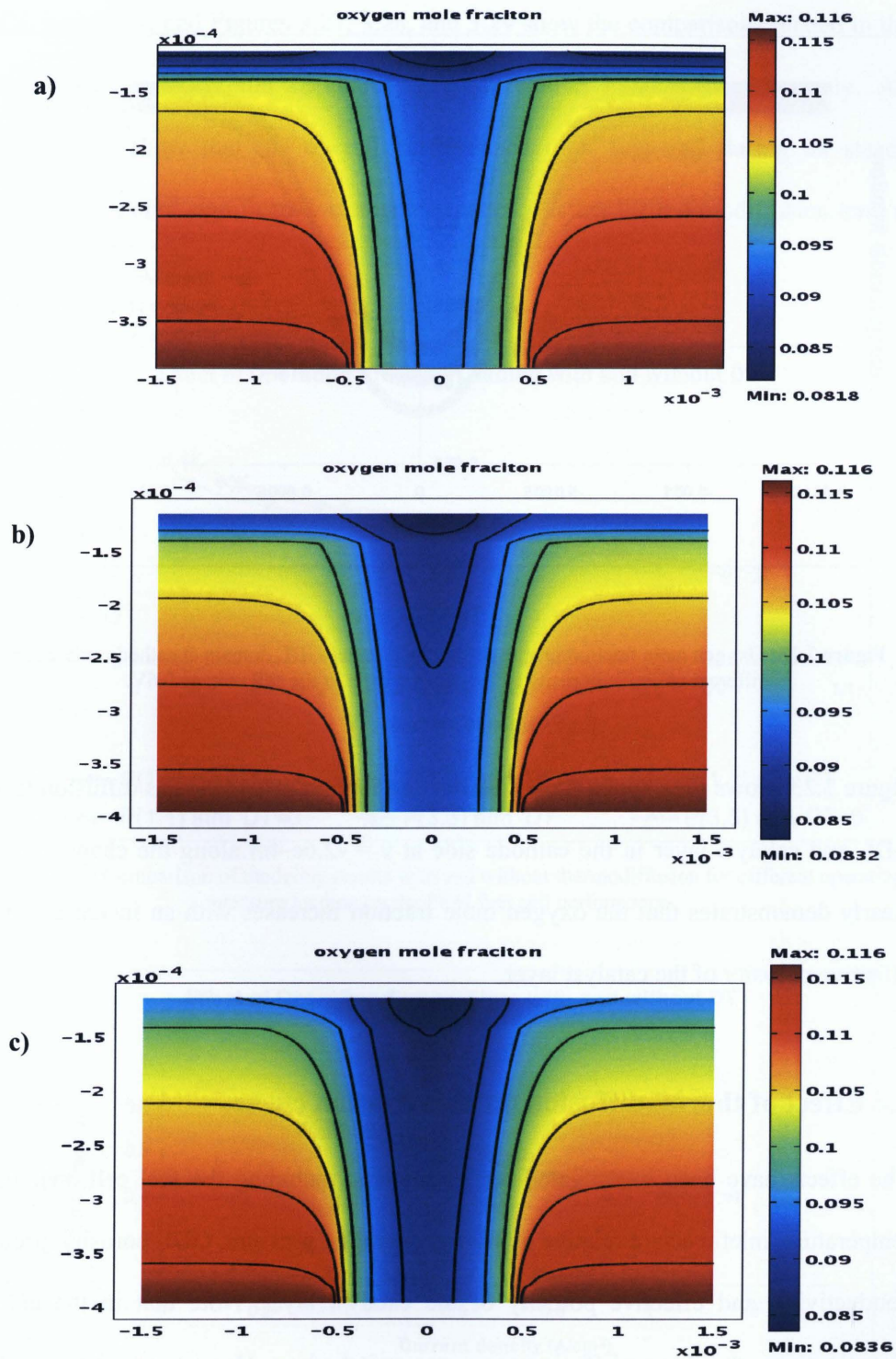


Figure 3.22: Oxygen mole fraction distribution in the cathode side with different effective porosity of the catalyst layer: (a) $\varepsilon_{ct} = 0.056$, (b) $\varepsilon_{ct} = 0.084$ and (c) $\varepsilon_{ct} = 0.14$ at cell voltage 0.6V.

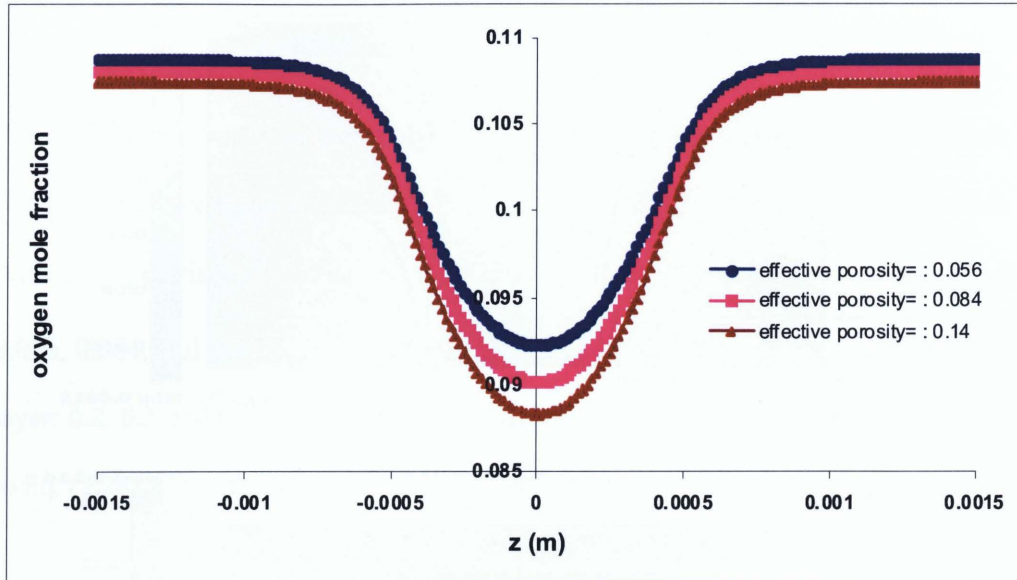


Figure 3.23: Oxygen mole fraction profile across the channel-GDL domain at cathode side under different effective porosity of the catalyst layer at the cell voltage 0.6V.

Figure 3.23 shows the oxygen mole fraction distribution across the gas diffusion layer GDL and catalyst layer in the cathode side at $y = -2.6e-4m$ along the channel. This clearly demonstrates that the oxygen mole fraction increases with an increase in the effective porosity of the catalyst layer.

3.4 Effect of thermodiffusion on polarization curve

The effects have been investigated for parameters, including the fuel cell operating temperature, inlet reactant relative humidity, operating pressure, GDL porosity, proton conductivity, and effective porosity of the catalyst layer. Note that in the above investigations, the thermodiffusion term was switched on. Here, a set of systematic comparisons are made against the results with the thermodiffusion effects turned off. Using the two types of simulation results, Figures 3.24 and 3.25 deal with the pressure loading and operating temperature, respectively; Figure 3.26 examines two different

GDL porosities; and Figures 3.27, 3.28, and 3.29 show the comparisons related to the effective porosity, proton conductivity, and relative humidity, respectively. All comparisons show that the overall performance of a fuel cell during its steady operation does not significantly change no matter whether the thermodiffusion term is switched on or off.

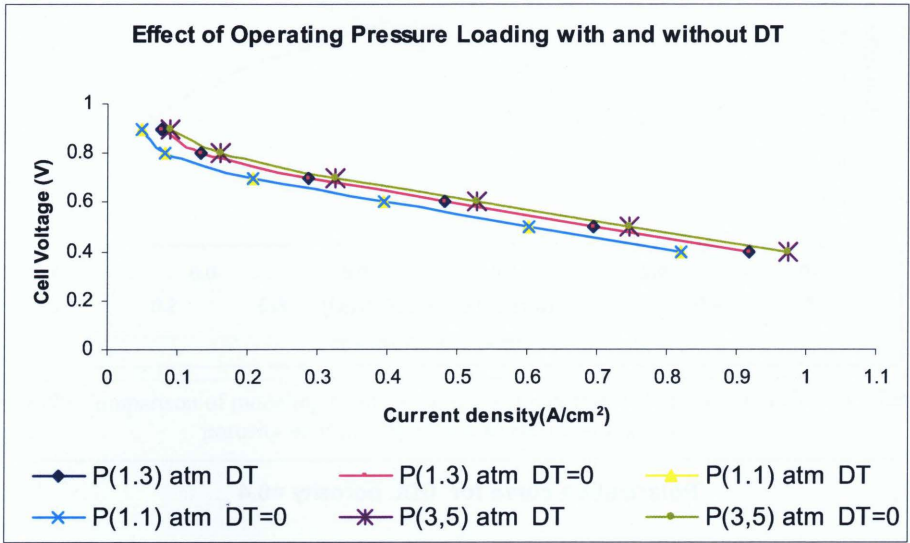


Figure 3.24: Comparison of modeling results with and without thermodiffusion for different operating pressure loading on the PEM fuel cell performance.

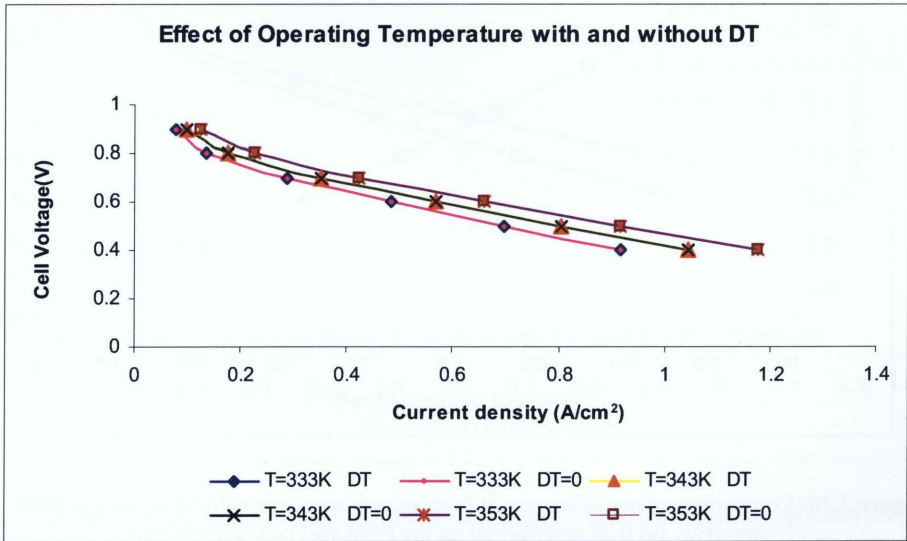


Figure 3.25: Comparison of modeling results with and without thermodiffusion for different temperature on the PEM fuel cell performance.

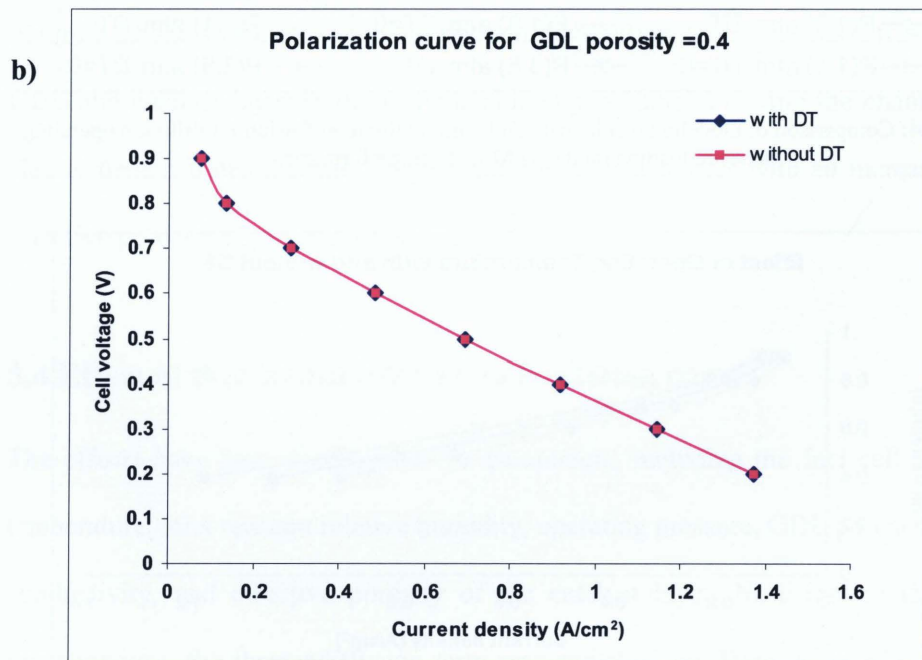
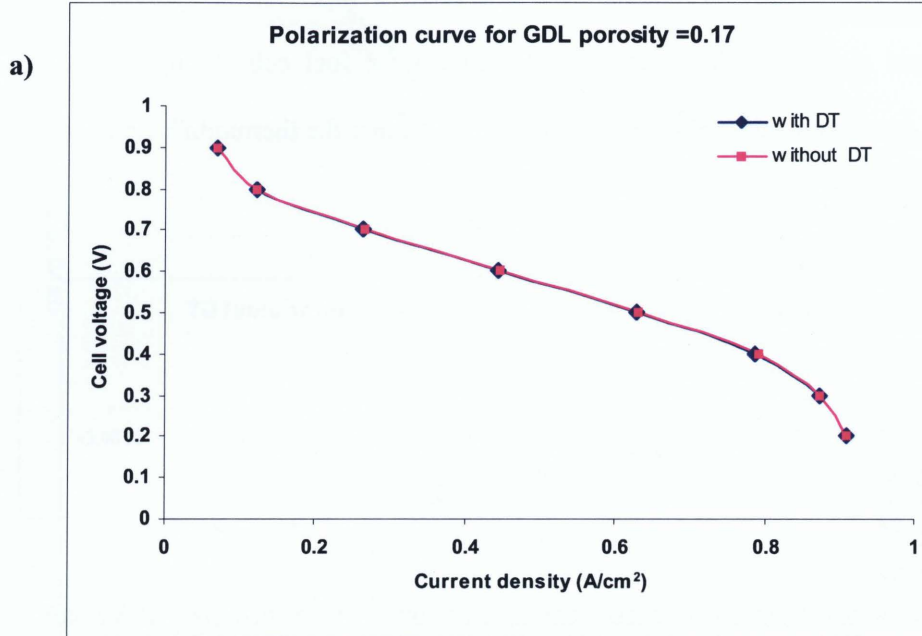


Figure 3.26: Comparison of modeling results with and without thermodiffusion for different GDL porosity: (a) 0.17 and (b) 0.4; on the PEM fuel cell performance

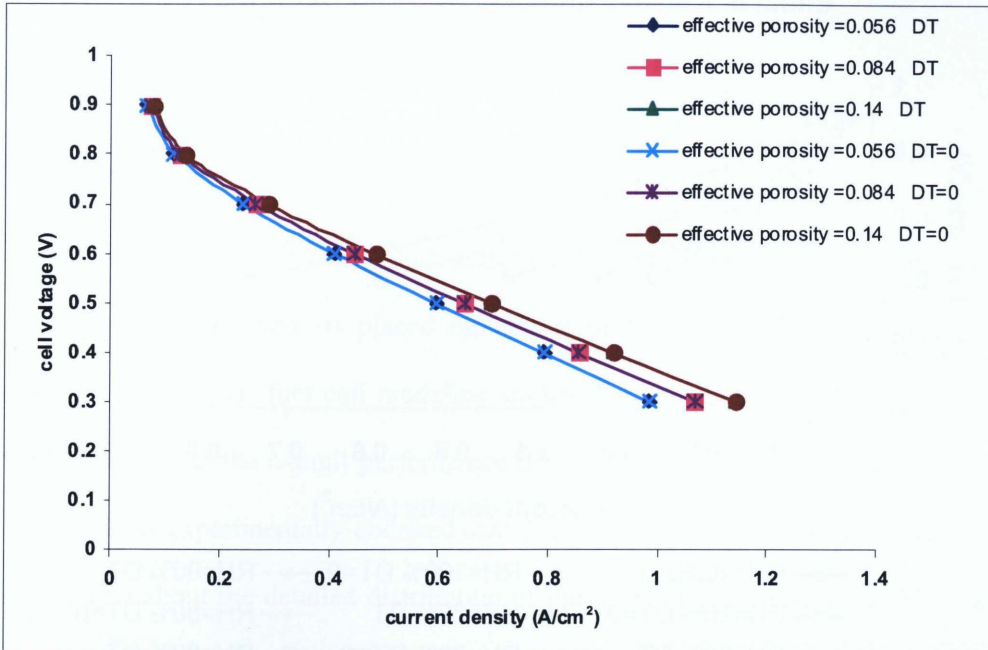


Figure 3.27: Comparison of modeling results with and without thermodiffusion for different effective porosity on the performance of the PEM fuel cell.

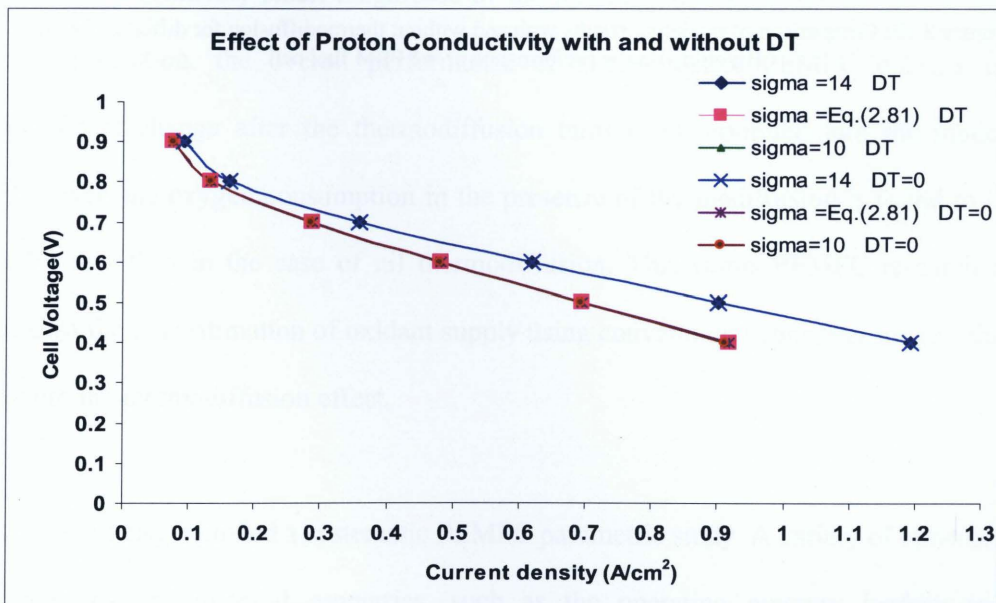


Figure 3.28: Comparison of modeling results with and without thermodiffusion for different proton conductivity on the performance of the PEM fuel cell.

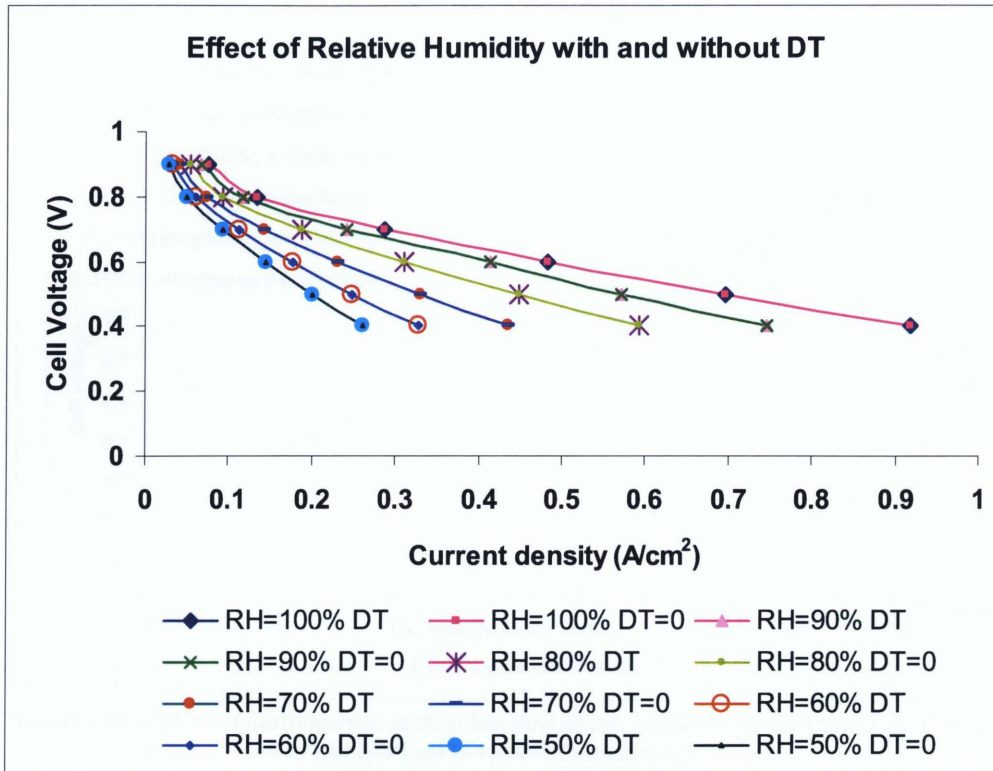


Figure 3.29: Comparison of modeling results with and without thermodiffusion for different Relative Humidity on the performance of the PEM fuel cell.

Chapter 4

Conclusions and Outlook

4.1 Conclusion

A two-dimensional, steady-state, and general-purpose PEMFC model was developed in this work with emphasis placed on effects of thermodiffusion that have been neglected in previous fuel cell modeling studies. The simulation based on this new model can predict the overall performance of PEMFC, which reach good agreement with available experimentally-obtained data. Simulation results also provided valuable information about the detailed distribution of the reactant gases inside the PEM fuel cell.

Due to the relatively small magnitude of the thermodiffusion coefficient in the fuel cell application, the overall performance of a steady-state PEMFC exhibits no significant change after the thermodiffusion term is incorporated into the model. However, the oxygen consumption in the presence of thermodiffusion is found to be 3.4% less than in the case of nil thermodiffusion. This warns PEMFC researchers against the overestimation of oxidant supply using conventional computer models that ignore the thermodiffusion effect.

This work also included a systematic PEMFC parametric study. A variety of operation conditions and material properties, such as the operating pressure loading and temperature, inlet reactant relative humidity, GDL porosity, proton conductivity, and effective porosity of the catalyst layer have all been tested. The results were presented

in the form of polarization curves, revealing that PEM fuel cells can perform better if using reasonably higher temperature, pressure drop, GDL porosity, effective porosity of catalyst layer and ensuring a full hydration of the cell.

The comprehensive fuel cell model developed in this study can be used to examine details of complex flow patterns, as well as mass and heat transport encountered in an operational PEMFC, which are usually unobservable by in-situ measurements due to the tiny dimension of the cell. The simulation results also provide insights that may assist practitioners in optimizing PEMFC design and reducing the manufacturing cost.

4.2 Contributions

Built upon previously established fuel cell models, refinements were made during this thesis work with the following new ingredients taken into consideration:

1. The new model was supplemented by incorporating the thermodiffusion term into the Maxwell-Stefan equations. This is an original piece of fuel cell research work since, as of today, none of other available PEMFC models have taken the thermodiffusion effect into account.
2. A detailed parametric study including the effective porosity of the catalyst layer was conducted using the refined model.
3. The Ohmic heating in electrodes can be examined in this new model, which made simulation results more realistic.

4.3 Recommendations

In order to render computer simulations more reliable, the PEM fuel cell model presented in this thesis may be improved by the following extensions:

1. Flow and mass transport are of two-phase nature in the fuel cell application, and this might have a great impact on the actual current profile at higher current densities. It is recommended to enable phase change in the fuel cell model to gain a more realistic understanding of the fuel cell operation mechanism.
2. Since the thermal gradient arises in all three directions for an operational fuel cell, a three dimensional model is recommended so that the non-isothermal effects can be fully pronounced in the simulation.
3. The model is established under the steady-state assumption, and this assumed condition prevents many effects, including the thermodiffusion effect, from evolving. Believing a transient model can provide more valuable insights to all types of overpotentials of the cell, it is strongly recommended to enrich, at the next stage, the present model by making variables time-dependent.

REFERENCE

- [1] Mikkola, Mikko. "Experimental Studies on Polymer Electrolyte Membrane Fuel Cell Stacks:" Helinski University of Technology, Department of Engineering Physics and Mathematics, *Masters Thesis*, 2001.
- [2] Leonard W. Fine, Herbert Beall, and John Stuehr: "Chemistry for Scientists and Engineers" *Preliminary Edition, Saunders Golden Sunburst Series*, 2000.
- [3] Colleen Spiegel: "Designing and Building Fuel Cells" *McGraw-Hills*, 2007.
- [4] Frano Barbir : " PEM Fuel Cells Theory and Practice." Elsevier Inc, 2005.
- [5] T. E. Springer, T. A. Zawodzinski, and S. Gottesfeld: "Polymer Electrolyte Fuel Cell Model" *J. Electrochemical Society*, Vol. 138(8), pp. 2334-2342, 1991.
- [6] D.M. Bernardi and M.W. Verbrugge: "Mathematical Model of a Gas Diffusion Electrode Bonded to a Polymer Electrolyte". *AIChE Journal*, Vol. 37 (8), pp.1151-1162, 1991.
- [7] V. Gurau, H. Liu, and S. Kakac: "Two-Dimensional Model for Proton Exchange Membrane Fuel Cells", *AIChE J*, 44(11), pp.2410-2422, 1998.
- [8] T. Zhou, H. Liu: "A General Three-Dimensional Model for Proton Exchange membrane Fuel Cells", *Int. J. Transport Phenom.*, 3, pp.177-198, 2001.
- [9] S. Um, C. Y. Wang: "Three-dimensional analysis of transport and electrochemical reactions in polymer electrolyte fuel cells, " *J. Power Sources* 125: pp. 40-50, 2004.
- [10] Paola Costamagna: "Transport phenomena in polymeric membrane fuel cells" *Chemical Engineering Science* 56, pp. 323-332, 2001.
- [11] Nedjib Djilali , Dongming Lu: "Influence of heat transfer on gas and water transport in fuel cells" *International Journal of Thermal Sciences*, Vol. 41(1), pp.29-40, 2002.

- [12] Christian Siegel: "Two-Dimensional, Non-Isothermal, Two-Phase Flow inside the Gas Diffusion Layer Unit of the Polymer-Electrolyte-Membrane Fuel Cell" *COMSOL Users Conference*, 2006.
- [13] J. Cao and N. Djilali: "Numerical modeling of PEM fuel Cells under partially hydrated membrane conditions" *ASME Journal of Energy Resources Technology*, Vol. 127(1), pp. 26-36, 2005.
- [14] Jianghui Yin: "Modeling and Simulation for a PEM fuel cell with catalyst layers in finite thickness" MAsc. thesis, Ryerson University, 2007.
- [15] Hao Wu: "Computational analysis on Proton Exchange Membrane Fuel Cell Technology" MAsc. thesis, Ryerson University, 2005.
- [16] T. Berning, D.M. Lu and N. Djilali: "Three-dimensional computational analysis of transport phenomena in a PEM fuel cell" *Journal of Power Sources*, Vol. 106, pp. 284-294, 2002.
- [17] Hong Sun, Hongtan Liu, and Lie-Jin Guo: "PEM fuel cell performance and its two-phase mass transport," *Journal of Power Sources*, Vol. 143, pp. 125-135, 2005.
- [18] L. You, H. Liu: "A two-phase flow and transport model for the cathode of PEM fuel cells" *International Journal of Heat Mass Transfer*, Vol. 45, pp. 2277-2287, 2002.
- [19] J. J. Baschuk and Xianguo Li: "A comprehensive, consistent and systematic mathematical model of PEM fuel cells" *Applied Energy*, Vol. 86(2), pp. 181-193, 2009.
- [20] Joseph O. Hirschfelder, Charles F. Curtiss and R. Byron Bird: "Molecular Theory of Gases and Liquids" *Kinetic Theory of gases-The Transport Coefficients* 8-9, 1976.
- [21] C.F. Curtiss and R.B. Bird: "Multicomponent Diffusion", *Ind. Eng. Chem. Res.* Vol. 38 (7), pp. 2515-2522, 1999.

- [22] Costeseque, P., Pollak, T., Platten, J. K., Marcoux, M.: “Simultaneous Evaluation of Soret and Fick Coefficients in a Free and a Packed Vertical Gradient Soret Cell” *6th International Meeting on Thermodiffusion*, IMT6, Varenna, Italy, 2004.
- [23] Ludwig, C., Sitzber, Akad, Wiss, Vien Math-Naturw., 20, p.539, 1856
- [24] Soret, C.: “Influence de la Temperature sur la Distribution des sels dans leurs Solutions,” *Acad. Sci., Paris, C. R.*, 91, pp. 289-291, 1880.
- [25] Ilya I. Ryzhkov: “On thermal diffusion and convection in multicomponent mixtures with application to the thermo gravitational column” *PHYSICS OF FLUIDS* 19, 027101, 2007.
- [26] R. Byron Bird, Warren E. Stewart and Edwin N. Lightfoot: “Transport Phenomena” *Second Edition*, 2002.
- [27] R. W. Schmitt: “Double diffusion in oceanography,” *Annu. Rev. Fluid Mech* Vol. 26, p. 255, 1994.
- [28] W. H. Furry, R.C. Jones, L. Onsager: “On the theory of isotope separation by thermal diffusion”, *Physical Review*, Vol. 55, pp. 1083-1095, 1939.
- [29] M. E. Schimpf: “Thermal field-flow fractionation,” in *Field-Flow Fractionation Handbook*, edited by M. E. Schimpf, K. Caldwell, and J. C. Giddings Wiley, New York, p. 239, 2000.
- [30] K. Ghorayeb, A. Firoozabadi: “Modeling multicomponent diffusion and convection in porous media” *SPE Journal*, Vol. 5(2), pp. 158-170, 2000.
- [31] Gholam Reza Z. Darvish, Erik Lindeberg, Jon Kleppe, and Ole Torsaeter: “Numerical Simulations for Designing Oil/CO² Gravity–Drainage Laboratory Experiments of a Naturally Fractured Reservoir,” Norwegian University of Science and Technology (NTNU), S.P. Andersensvei 15 a, NO-7491 Trondheim, Norway.

- [32] S.R. de Groot : Theorie phenom_enologique de l'effet Soret, *Physica*, Vol. 9(7), pp. 699-708, 1942.
- [33] S.R. de Groot, P. Mazur, "Non Equilibrium Thermodynamics," *North-Holland Publishing Company, Holland*, 1962.
- [34] J.K. Platten: "The Soret Effect: a review of recent experimental results" *Journal of Applied Mechanics*, Vol. 73, pp. 5-15, 2006.
- [35] G. Gagan, "Flow and Transport in Porous Formation", *Springer-Verlag, Berlin*, 1989.
- [36] G.H. Guvelioglu and H.G. Stenger: "Computational fluid dynamics modeling of polymer electrolyte membrane fuel cells" *Journal of Power Sources*, Vol. 147(1-2), pp. 95-106, 2005.
- [37] R. Krishna: "Problems and Pitfalls in the Use of the Fick Formulation for Intraparticle Diffusion" *Chemical Engineering Science*, Vol. 48(5), pp. 845-861, 1993.
- [38] C. F. Curtiss and J.O. Hirschfelder: "Transport properties of multicomponent gas mixtures", *Journal of Chem. Phys.*, 17, pp. 550-555, 1949.
- [39] G.A. J. Jaumann Wien. Akad: "Closed system of physical and chemical differential laws", *Sitzungsberichte (Math-Naturw.Klasse)*, 120, 2a, pp. 385-530, 1911.
- [40] D. M. Bernadi and M. W. Verbrugge: "A Mathematical model of the solid Polymer electrolyte fuel cell" *Journal of Electrochemical. Society*, Vol.139 (9), pp. 2477-2491, 1992.
- [41] K.K.Y. Kuo, *Principles of Combustion: First edition*, John Wiley, and Sons, New York, 1986.

- [42] P.D. Beattie, F.P. Orfino, V.I. Basura, K. Zychowska, J.F. Ding, C. Chuy, J. Schmeisser, S. Holdcroft: "Ionic conductivity of proton exchange membranes" *Journal Electroanalytical Chemistry*, Vol. 503(1-2), pp. 45-56, 2001.
- [43] D. Singh, D. M. Lu, and N. Djilali: "A Two-Dimensional Analysis of Mass Transport in Proton Exchange Membrane Fuel Cells" *International Journal of Eng. Sci.*, Vol. 37, pp. 431-452, 1999.
- [44] M. W. Verbrugge and R. F. Hill: "Ion and Solvent Transport in Ion-Exchange Membranes" *Journal of Electrochemical Society*, Vol. 140(5), pp. 1218-1225, 1993.
- [45] T. Zhou and H. Liu: "Effects of the electrical resistance of the GDL in the PEM fuel cell" *Journal of Power Sources*, Vol. 161(1), pp. 444-453, 2006.
- [46] H. Ju, and C.Y. Wang: "Experimental Validation of a PEM Fuel Cell Model by Current Distribution Data" *Journal. Electrochemical Society*, 151(11): pp. 1954-1960, 2004.
- [47] COMSOL Multiphysics User's Guide, COMSOL 3.3., 2006.
- [48] L. Wang, A. Husar, T. Zhou, H.Liu: "A Parametric Study of PEM Fuel Cell Performances" *International Journal of Hydrogen Energy*, Vol. 28, pp. 1263-1272, 2003.
- [49] Qiangu Yan, Hossein Toghiani, Junxiao Wu: "Investigation of Water Transport through Membrane in a PEM Fuel Cell by Water Balance Experiments" *Journal of Power Sources*, Vol. 158, pp. 316-325, 2006.
- [50] D. Natarajan and T.V. Nguyen: "Three-dimensional effects of liquid water flooding in the cathode of a PEM fuel cell" *Journal of Power Sources*, Vol. 115(1), pp. 66-80, 2002.

- [51] T. Berning, N. Dijiali: "A 3D, multiphase, multicomponent model of the cathode and anode of a PEM fuel cell" *Journal of Electrochemical Society*, Vol. 150(12), pp.1589-1598, 2003.
- [52] Gottesfeld, S. and T. A. Zawodzinski: "Polymer Electrolyte Fuel Cells, in R. C. Alkire, H. Gerischer, D. M. Kolb, and C. W. Tobias (editors)" *Advances in Electrochemical Science and Engineering*, Vol. 5 (Wiley-VCH, New York, 1997).